Material fingerprinting as a tool to investigate between and within material type variability with a focus on material hardness

van Duijvenbode, Jeroen R.; Cloete, Louis M.; Shishvan, Masoud S.; Buxton, Mike W.N.

DOI
10.1016/j.mineng.2022.107885

Publication date
2022

Document Version
Final published version

Published in
Minerals Engineering

Citation (APA)
van Duijvenbode, J. R., Cloete, L. M., Shishvan, M. S., & Buxton, M. W. N. (2022). Material fingerprinting as a tool to investigate between and within material type variability with a focus on material hardness. *Minerals Engineering*, *189*, Article 107885. https://doi.org/10.1016/j.mineng.2022.107885

Minerals Engineering 189 (2022) 107885

Contents lists available at ScienceDirect

Minerals Engineering

journal homepage: www.elsevier.com/locate/mineng

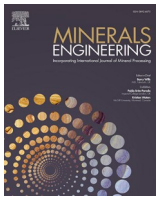

Material fingerprinting as a tool to investigate between and within material type variability with a focus on material hardness

Jeroen R. van Duijvenbode [a,*], Louis M. Cloete [b], Masoud S. Shishvan [a], Mike W.N. Buxton [a]

[a] Resource Engineering Section, Department of Geosciences and Engineering, Delft University of Technology, Stevinweg 1, 2628 CN Delft, The Netherlands
[b] AngloGold Ashanti, Johannesburg, South Africa

ARTICLE INFO

Keywords:
Tropicana Gold Mine
Material fingerprinting
Block feature clustering
Geometallurgy
pXRF
VNIR-SWIR spectroscopy

ABSTRACT

Geochemical and mineralogical datasets from Tropicana Gold Mine, Australia, have been used to define Au-mineralised fingerprints. VNIR-SWIR spectral data were represented by four normalised wavelength regions and were clustered to form spectral classes. Sequentially, these spectral class proportions within a block and co-located pXRF data were clustered to discriminate material types (fingerprints). The hardness of each type was further explored using collocated BWi, Axb, Equotip rebound hardness and penetration rate datasets, but also by considering spatial contextual relationships and the within material type variability. The Tropicana orebody example gave a good illustration of how a phengitic-epidote K-feldspar rich domain (schistosity and softer, ~15–18 kWh/t) separated from a harder (>20 kWh/t), shorter wavelength phengitic plagioclase-rich feldspar dominated domain. Exploring the within material type differences using the white mica composition (wAlOH) and a new w605 spectral feature demonstrated how the effects of shearing were captured within material types. Such findings will ultimately improve the understanding of the constitutive material hardness and have significance for process optimisation and blending strategy design.

1. Introduction

Traditionally, the mining industry tends to concentrate on testing, understanding and domaining rock hardness within orebodies (e.g., crushability and grindability) during focused metallurgical studies. However, the hardness is of significant importance for informing strategic and tactical geometallurgical decisions, such as comminution circuit design and forecasting throughput during the life of mine (Dominy et al., 2018). In this context, hardness refers to the resistance of a material to deformation, indentation, penetration or deformation by means such as abrasion, drilling, impact, scratching or wear (Lynch, 2015). Provided this importance, it is interesting that the material hardness itself is commonly only understood by doing additional hardness tests (Michaux and O'Connor, 2020) or by modelling its spatial abundance (Deutsch et al., 2015). Another issue is the large quantity of material required for the most common comminution tests and their high associated costs. Unfortunately, this limits the number of tests conducted and confines the understanding of the full range of metallurgical properties from the deposit. As a result, typically only preliminary hardness modelling is done based upon the mineralogical, metallurgical and comminution test results retrieved during feasibility studies (see, for example, King and Macdonald (2016); Montoya et al. (2011)). However, only limited efforts are made to determine why and how the geology impacts the material hardness.

The material hardness of an orebody is encountered during drilling, testing, loading and comminution processes. The dominant processes controlling rock hardness occurred between ca. 2640–1140 Ma in the case of this study's orebody (Blenkinsop and Doyle, 2014), and only slightly changed over time in the case of weathering at shallow surfaces (Ogunsola et al., 2017). The hardness is defined by, for example, *meso-* and microscale shear zone kinematics (faults, folds, shearing), rock massiveness (grain size distribution), unconformities, deformations, crystallisation, metamorphism, textural changes or the physical hardness of the constituent minerals. At the Tropicana Gold Mine, biotite with pyrite and gold-bearing assemblages (at other parts, biotite-sericite and minor chlorite) crystallised in shear zones within K-feldspar-rich pegmatitic rocks (during D3 deformation following Blenkinsop and Doyle (2014)). This deformation postdates the formation and folding of a gneissic fabric but predates overprinting by other phyllosilicates through new shear zones from later deformation events comprising dextral shearing (D4, D5 shear zones and folds, Blenkinsop and Doyle (2014)). This deformation history example contains several phases in

* Corresponding author.
E-mail address: j.r.vanduijvenbode@tudelft.nl (J.R. van Duijvenbode).

https://doi.org/10.1016/j.mineng.2022.107885
Received 14 January 2022; Received in revised form 16 September 2022; Accepted 10 October 2022
Available online 26 October 2022

which the material hardness has changed, but implies that when a fingerprint of material can characterise or domain hydrothermal mineral phases (Molnár et al., 2017; Roache, 2019), fluid pathways in shear zones (Hood et al., 2019) or deformation events (Blenkinsop and Doyle, 2014), then the fingerprinting can also describe the hardness variability.

The concept of material fingerprinting entails that a fingerprint is a material classification based on the similarity of the measured and constitutive material attributes (van Duijvenbode et al., 2020). Ideally, these fingerprints are a better proxy for the constitutive hardness properties found within a small spatial area or domain (representing a material blend) compared to those of individual samples. Various geometallurgical case study examples follow the same principles but with different aims and considered datasets. For example, van Duijvenbode et al. (2022) explore the relationship between four acid digestion data and the Bond Ball Mill Work Index (BWi) and recovery. Bhuiyan et al. (2022) demonstrate that a portable X-ray Fluorescence (pXRF) to BWi relationship is favoured. Wambeke et al. (2018) demonstrate the use of such a relationship in real-time reconciliation of BWi, whereas, in Johnson et al. (2019), the mine favours a Visible Near Infrared – Short Wave Infrared (VNIR-SWIR) hyperspectral imaging application to predict recovery and throughput. Other studies show fingerprinting of solely VNIR-SWIR mineralogy along drill holes (Abweny et al., 2016; Arne et al., 2016; Kazimoto, 2020) or mineralised outcrops (Booysen et al., 2022).

The main aim of this paper is to use material fingerprints to understand and determine a relationship for between- and within material type differences by focussing on the measured hardness. Demonstration of such an outcome could assist in optimal sample selection, comminution design or give insights towards reducing energy consumption. This will be done by firstly demonstrating the construction of material fingerprints for mining blocks using grade control (GC) point-data sources (pXRF and VNIR-SWIR measurements), secondly explaining the rock attributes for each material type, and thirdly demonstrating spatial contextual relationships of the material types with hardness and alteration mineral assemblages. This will be tested and validated by linking each fingerprint with the typical BWi, Axb, Equotip and penetration proxy parameters characterising the comminution behaviour of this material. Finally, it is shown how the learnt fingerprint (material type) to work index relationships can be improved by exploring the within material type variability.

2. Geology and mineralisation

The Tropicana Gold Mine (TGM) is situated in the Plumridge Terrane, a zone that separates the in situ eastern margin of the Yilgarn craton from the Albany-Fraser orogen, Western Australia (Fig. 1a). This gneissic terrane consists of Archean crust (2.7 Ga) and is strongly modified by amphibolite to granulite facies grade metamorphism (Doyle et al., 2015). Closer to the mine, the granulite facies quartzofeldspathic gneisses are highly deformed and truncated by moderately east to southeast dipping shear zones. Post mineralisation faulting resulted in four distinct structural domains, which are from north to south: Boston Shaker, Tropicana, Havana (including Havana Deeps) and Havana South (Fig. 1b). Most economic gold mineralisation occurs within high gold grade shoots, including the southeast plunging mineralised zones at Boston Shaker, Tropicana NE, Havana and Havana South.

The deposit was formed by fluid flow through a network of biotite-pyrite-bearing shear zones and is hosted within a sequence of high-grade quartzofeldspathic and garnet-bearing gneisses, with amphibolites, granulites, metasedimentary cherts and pegmatites (Fig. 2). These mineralised zones occur as one or two laterally extensive planar lenses with a moderate dip. The favourable host to mineralisation is a preferentially deformed feldspathic gneiss facies (Crawford and Doyle, 2016; Hardwick, 2021). The framework silicate modal mineralogy within this unit consists of perthitic K-feldspar and plagioclase-rich end-members (Hardwick, 2021). Perthitic K-feldspar rich end-members have a higher K/Al (molar) ratio than the plagioclase-rich end-members. Within the mineralised zone, biotite, sericite, and pyrite alteration replaced the metamorphic mafic minerals and feldspar (Blenkinsop and Doyle, 2014; Crawford and Doyle, 2016).

Fig. 3 shows an example of a feldspathic gneiss unit having intervals of sericite-biotite, biotite-pyrite and sericite-biotite-chlorite alteration. The mineralised rock exhibits significant enrichment in S and the ore elements (Mo, Te, Tl, Ag, Au, W) and K-group elements (K, Rb, Hf, Zr, U). Previous work by the authors (van Duijvenbode et al., 2022) highlighted significant relationships between lithology and material hardness based on four acid digestion multi-element data. This suggests that the pXRF and VNIR-SWIR data used in this study would also represent these material attributes.

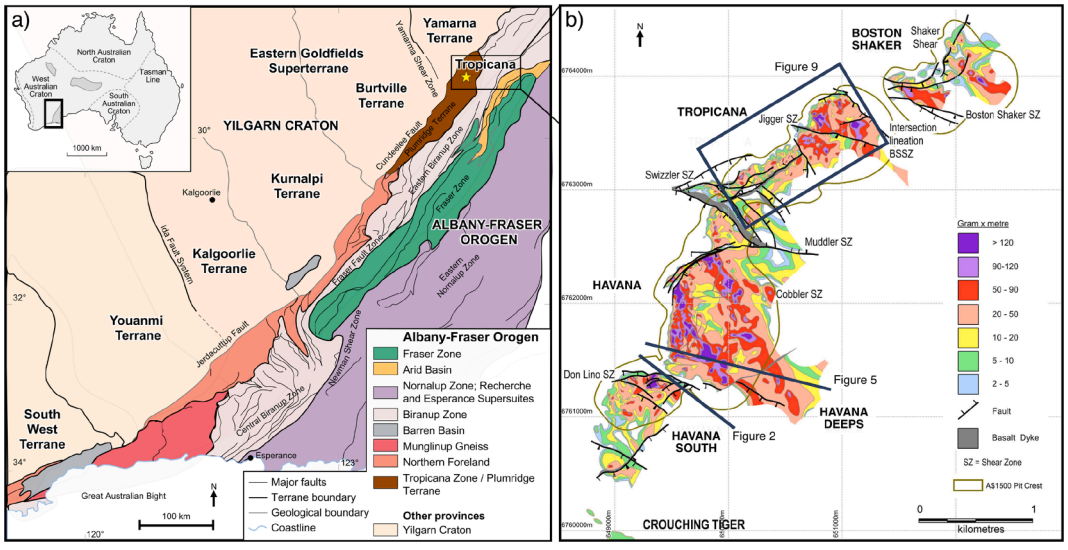

Fig. 1. (a) Geological map of the Albany-Fraser Orogen with respect to the eastern margin of the Yilgarn Craton, Western Australia, showing the location of the Tropicana gold deposit. Modified after Spaggiari et al. (2011); (b) Structural domains and shear zones superimposed on a grade (g/t) × thickness (m) plot. GDA94 / MGA zone 51 grid. Modified after Blenkinsop and Doyle (2014).

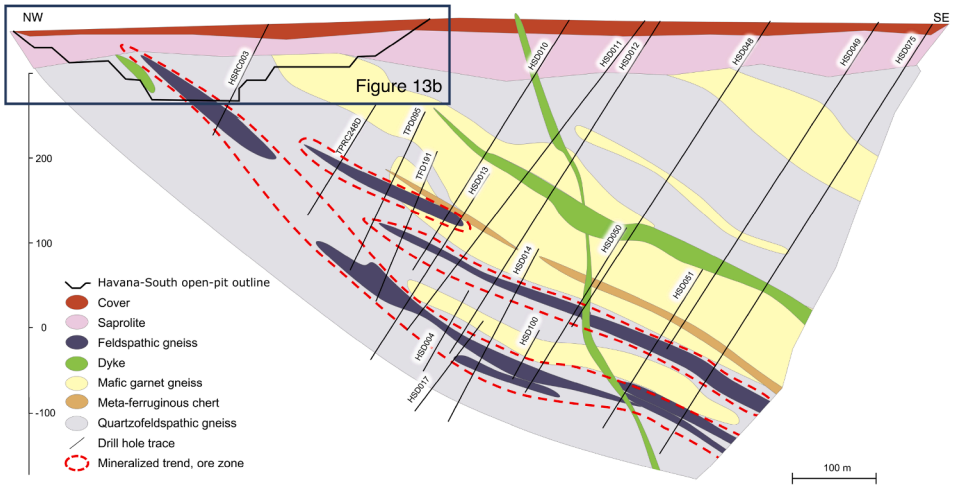

Fig. 2. Schematic NW-SE cross-section of the Havana South deposit (100 m thick at 649,753 mE, 6,761,137 mN, azimuth 37°, GDA94 / MGA zone 51 grid), after van Duijvenbode et al. (2022).

3. Methods

Data were obtained from several Tropicana Gold Mine (TGM) sources. Most of the mineralogical (VNIR-SWIR, $n = 128{,}584$) and geochemical data (pXRF, $n = 162{,}398$) were collected from co-located GC drilling samples, others originated from exploration drill hole samples. These samples represent the geochemical and mineralogical variability within the $\geq$ 0.3 ppm Au grade resource modelling domains. Most of these measurements were taken on drill chips and pulps from GC drilling and, therefore, had a dense spatial resolution (typically 6x6 m or 9x9 m). The resulting 1 m samples were sent to an on-site laboratory for analysis. The hardness data will be discussed in Section 3.3.

The preparation workflow of this study is schematically summarized in Fig. 4 and consists of two parts. The first part prepares a block model ($12 \times 12 \times 3$ m) containing geochemical (Section 3.1) and mineralogical data (Section 3.2) attributes. However, two problems had to be overcome. Firstly, geospatial modelling of VNIR-SWIR features is not as common as modelling geochemical data (e.g., using kriging). Therefore, an additional preparation step of the mineralogical data is proposed to create a categorical variable indicating the type of mineralisation of a sample. This consists of agglomerative hierarchical clustering of the spectral responses as outlined in Section 3.2 and gives the spectral or mineralogical class indicator which can be assigned to the sample. Secondly, the modelling itself is a problem as the variety and scale of data obtained from different sample measurements (including the to-be-considered hardness data) complicates merging datasets. To overcome this challenge, all samples were assigned to the nearest block from the $\geq$0.3 ppm Au grade resource modelling block model from the mine based on their spatial location. These samples within a constrained block volume should, given their spatial proximity, relate to each other (material blend). Subsequentially, only blocks with sufficient samples were considered for further analysis (block feature clustering), and no spatial modelling of attributes was required. Finally, a spatially dense block model was still obtained due to the vast number of samples and spatially dense GC drilling grid.

The second part involves clustering block features into material types and analysis with hardness proxies. As a result of the first part, most samples had a set of elemental concentrations and an assigned spectral class obtained through the clustering. Note that some samples only had VNIR-SWIR measurements, and others only pXRF measurements. The block feature clustering approach aims to increase the spatial resolution and context of the sample results. This will result in a block model where each block with sufficient data (no simulation done) in the mine plan is valued not only on Au grade but on a combination of the 15 elements and VNIR-SWIR data (the block features). The resulting material attribute classification will then become a proxy for the comminution indices. This allows for scale-up from sample to block; all individual samples within a block were merged and further prepared for block feature clustering by the following steps:

1. Average the elemental concentrations to get a unique geochemical signature per block. Since pXRF data are compositional in nature, they require a further transformation to log-ratio coordinates to account for closure (Aitchison, 1999). Therefore, the concentrations are transformed using a centred log-ratio (clr). This transforms the data coordinates from the simplex, an *n*-dimensional composition within the positive real number space, to the Euclidean real space more suitable for statistical analysis (Aitchison, 1986). Note that the clr transformation is done using all block geochemical signatures and not per block.
2. Determine the proportion of each spectral class (Section 3.2) based upon all classes found within a block. These class proportions are useful as they provide a quantitative description of the mineralogical blend characteristics.
3. Combine the spectral class proportions and pXRF features and normalise by a z-score transformation to obtain values in a similar range.
4. Reduce the feature dimension of these block features (spectral class proportions and pXRF clr-transformed concentrations) using PCA. The number of PCs is automatically set to the amount that can describe 95 % of the data variance.
5. Cluster the block features PC dataset using agglomerative hierarchical clustering to partition the blocks into clusters (Wierzchoń and Kłopotek, 2018). The algorithm starts with each block as an individual cluster. Next, pairs of clusters are successively merged based upon similarity until all clusters have been merged into one big cluster containing all blocks. These clusters represent so-called "*material types*" with similar mineralogical and geochemical attributes. Note that the mineralogical data (Section 3.2) is clustered using the same clustering technique.

The final block material type (fingerprint) is a combination of pXRF elemental concentrations (Section 3.1) and a separate VNIR-SWIR data clustering approach (Section 3.2). The initial assumption is that geochemistry and mineralogy then largely explain the legacy material hardness parameters and constrain distinct hardness domains.

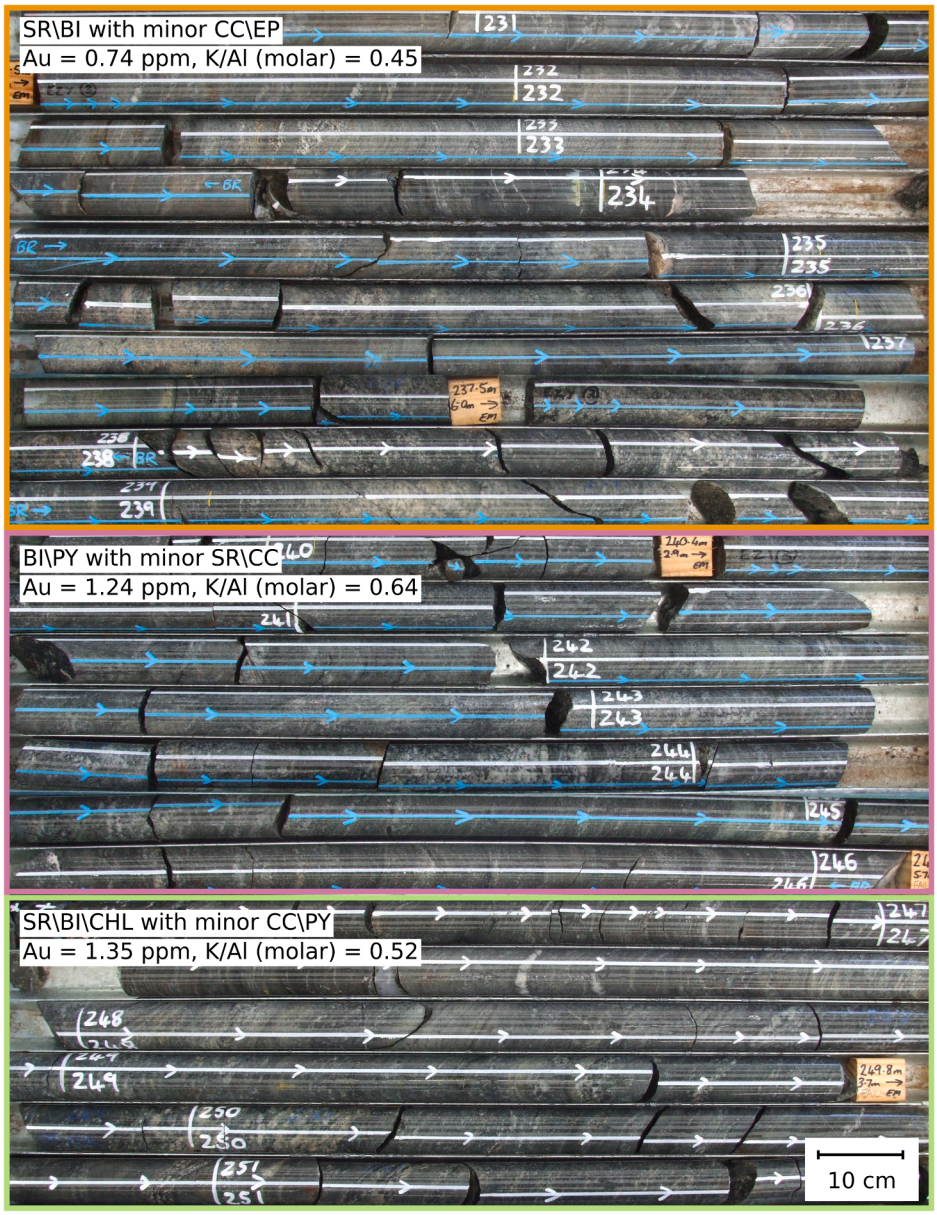

Fig. 3. Core tray photographs of plagioclase (lower molar K/Al) and perthitic K-feldspar rich (higher molar K/Al) feldspathic gneiss domains with distinct zones of alteration. SR: sericite, BI: biotite, PY: pyrite, CHL: chlorite, CC: calcite, EP: epidote. Drill hole TPD234 from 231 to 252 m depth.

3.1. Geochemical data

The geochemical dataset (n = 162,398 samples) used in this study originates from portable XRF (pXRF) measurements taken on samples from within the ≥0.3 ppm Au grade resource modelling domains. The bulk concentrations of the following (15) elements were considered: Al, Ca, Cr, Fe, K, Mn, Nb, Pb, Rb, S, Si, Sr, Ti, Zn and Zr. Other elements including Ag, As, Bi, Cl, Co, Cu, Mo, Mg, Ni, Se, V and W were not considered because >50 % of their values reported under the detection limit. In addition, the samples were assayed for gold using a 50 g charge fire-assay and subsequently analysed by solvent extraction Atomic Absorption Spectroscopy (AAS). The Au concentration was not used in the clustering as this ensures that emphasis is placed on major and other trace elements for classification (van Duijvenbode et al., 2022). The gold concentration is only used in this study to help interpret the different material types and constrain the domains. Fig. 5 shows an example of the geochemical data and indicates how the Au, Zr, K and S concentrations can be used to characterise the hanging (HW) and footwall (FW) ore zones, dominantly hosted in felsic gneiss of the Havana deposit, and how the geochemistry changes with depth. It also shows, that the non-Au elements will be deterministic in identifying zones of various geochemical composition related to Au mineralisation.

Since inception of the Tropicana Gold Mine operation, samples have been analysed in an on-site laboratory using an automated sample preparation circuit where both pXRF and VNIR-SWIR data are routinely captured. The laboratory adheres to routine data checks, which renders further quality control before conducting this research redundant. These controls include routine certified reference material (three per hundred samples), blank (first sample in each laboratory job and into the sequence of samples before each zone of mineralisation), repeat and duplicate measurements. QA/QC results are reviewed on a batch-by-batch and monthly basis. Any deviations from acceptable precision or bias indicators are acted on with repeat and check assays (AngloGold Ashanti, 2016). In addition, the number of samples (n = 162,398) used in this study likely reduces statistical errors and renders the database resilient for errors.

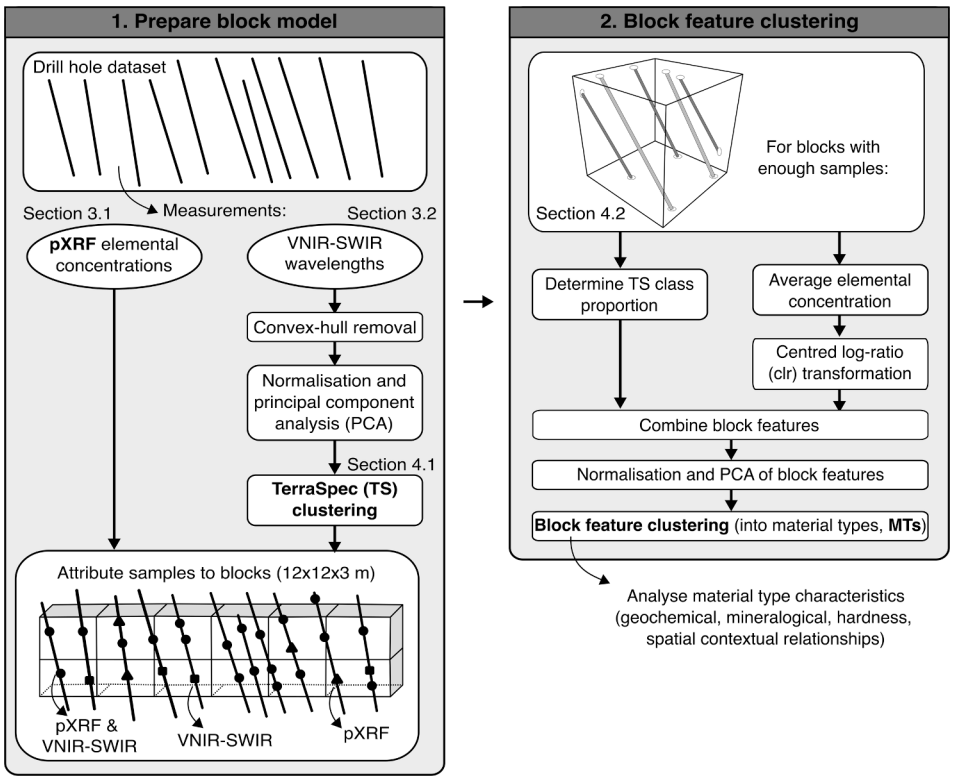

Fig. 4. Schematic workflow of the block model preparation and block feature clustering approach.

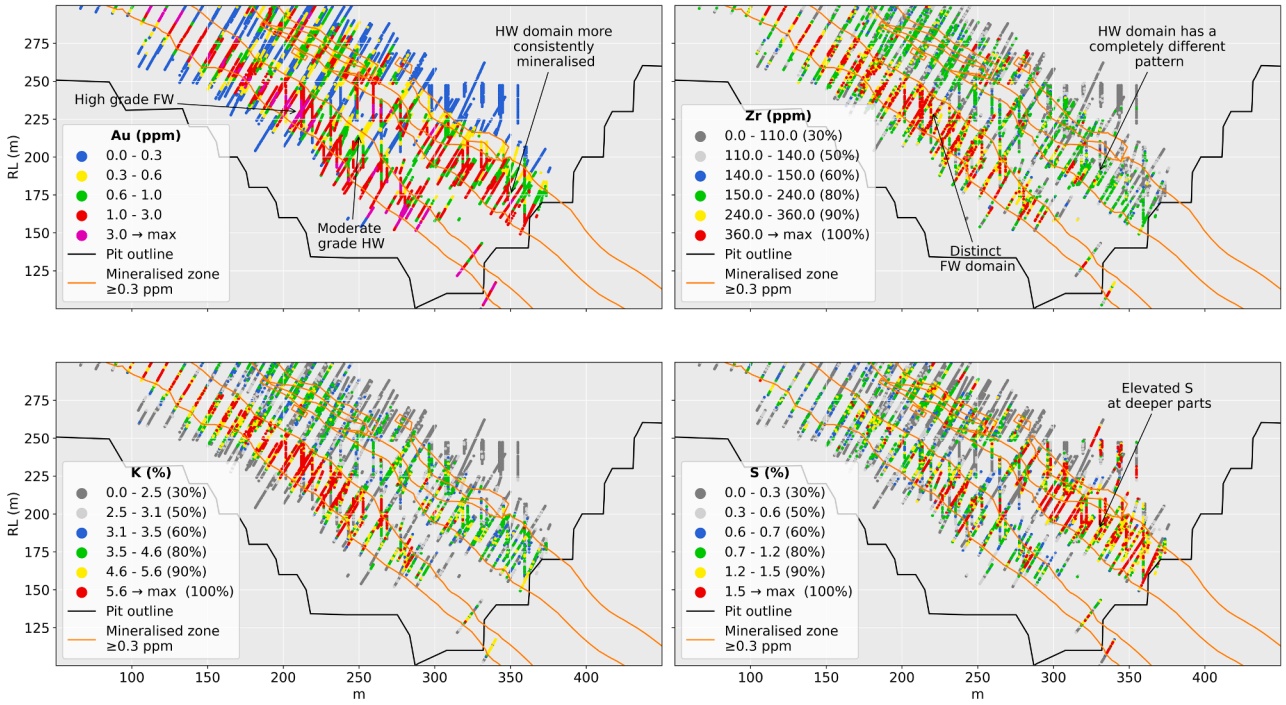

Fig. 5. pXRF concentrations of Au, Zr, K and S in relation with the hanging (HW) and footwall (FW) lodes at Havana (50 m thick cross-section). The block feature clustering approach only considers samples within the modelled mineralised zone.

3.2. Mineralogical data

The mineralogical dataset consists of 128,584 spectral measurements on samples from within the ≥0.3 ppm Au grade resource modelling domains. The measurements were taken using an ASD TerraSpec mineral spectrometer (hereafter referred to as TS data), and each spectral response covers the reflectance of the electromagnetic spectrum at the VNIR and SWIR regions (350–2500 nm). Processing and interpretation of the results were undertaken using two processes. The first process uses unprocessed spectral responses, whereas the second process

uses a standard suite of absorption features typical for gold systems.

The first process aims to use unsupervised learning (clustering) to generate classes of mineralogically similar samples. The clustering uses "raw" or unprocessed spectral responses as input and, therefore, omits the need for mineralogical identification and absorption feature creation (Ausspec, 2008; Rodger et al., 2021). Additionally, using uninterpreted spectra may reveal hitherto unknown textural or hardness signatures not recognised or identified before. Each spectral response was prepared by subdividing the wavelength range into four sub-regions: 500–750 nm, 1300–1450 nm, 1850–2000 nm and 2150–2400 nm. Fig. 6a shows a typical TS spectrum with the four regions of interest highlighted. These regions were selected because they contain the most spectral variability. The selected regions and corresponding typical spectral response (Ausspec, 2008) are described in Table 1. In terms of identifying and characterising the white mica composition, the 2150–2400 nm region is of particular interest for two reasons. Firstly, the wavelength of a diagnostic Al-OH absorption feature between 2180 nm and 2228 nm (wAlOH) defines the white mica composition and is thus useful for spatial mapping of mineralised domains. For example, a muscovite white mica corresponds with the lower wavelengths (<2216 nm) and phengitic white mica to higher wavelengths (>2216 nm). Phengite at TGM is especially closely spatially associated with gold and shear zones controlling lode geometry (Roache, 2019). This can, for example, differentiate K-feldspar-dominated domains (higher work index, harder) from mica-dominated domains (lower work index, softer). Secondly, the abundance (depth at 2205 ± 25 nm, dAlOH) can then be used to differentiate the feldspar vs sericite composition.

The spectral response in each region was smoothed and normalised by a convex-hull removal (CHR) to remove dependence upon reflectance. This ensures that the spectra can be compared because the absorption features are purely a function of depth and width (Ausspec, 2008). The benefit of this approach can be seen in the 500–750 nm region, as will be discussed in Section 4.5. Usually, these predominantly iron-related features are depressed because the convex hull removal over the entire spectrum. However, doing this across a smaller region preserves features and may magnify their expression (Fig. 6b).

The data from each region were combined, and each wavelength feature ($n = 800$) was normalised by removing the mean and scaling to unit variance. Then, the feature dimension was reduced by principal component analysis (PCA). The number of principal components (PCs) was automatically set to the amount which describes 95 % of the data variance. Finally, the lower-dimensional dataset functions as input for a clustering algorithm. This study used an agglomerative hierarchical clustering approach (Wierzchoń and Kłopotek, 2018) but, in addition other algorithms were tested (K-means, density based methods). After clustering, each sample is assigned a class label related to a specific suite of mineralogical signatures occurring within the four wavelength regions.

The second process uses The Spectral Geologist (TSG; Version 8.0.7.4, CSIRO, Perth, WA, Australia) software to provide quick and reliable interpretations of predefined mineralogical features (Laukamp et al., 2021). These spectral interpretations were assumed to be valid since they are generally used in-house, having been refined over many years. The main proxies considered are described in Table 1. This process is primarily used to provide mineralogical interpretation to the classes from the first clustering process. In addition, these results may capture signatures from the regions not considered above.

3.3. Material hardness proxy data

After analysing the geochemical and mineralogical results of the material types, the focus shifted to the hardness characteristics of each identified material type. These characteristics were identified using the following four legacy hardness proxy datasets jointly:

- Equotip rebound hardness measurements (unit is Leeb, Ls) were primarily taken on diamond drill core with intervals of one metre. Generally, ten measurements were taken per sample, and for this study, simply the median value was chosen to give one data point per meter. This hardness value is calculated from the impact and rebound speed ratio and typically reflects the mineralogical rebound hardness based on the observed matrix crystal structure. A higher Leeb corresponds with a harder sample.
- The Bond Ball Mill Work Index (BWi in kWh/t) and the JK rock breakage parameters (Lynch, 2015) expressed as comminution index Axb, were infrequently collected on diamond drill cores during metallurgical testing campaigns. The BWi reflects the combined resistance to abrasion and impact, whereas Axb reflects the compression resistance. Higher values of BWi indicate harder ore, whereas higher values of Axb indicate a decreased hardness.
- The penetration rate (m/hr) was directly derived from the time required to drill through a one-meter rock mass. When machine operating conditions are kept constant, this represents a material hardness indicator since the parameter is collected continuously along every hole drilled. This study considered only penetration rates from GC drilling of ~10–12 m long blast holes. Lower values indicate harder rock mass since the material takes longer to penetrate, and therefore delivers less drilled meters per hour.

4. Results

4.1. VNIR-SWIR clustering

PCA reduced for 128,584 samples the 800 wavelength features derived from the four regions to nineteen features (accounting for 95 % data variance). In this context, each PC represents a combination of features visible in the hull normalised spectra of the four wavelength regions. Fig. 7 displays PC1 is accountable for 25 % of the data variance, and that a positive PC1 is mostly related to the 1405–1448 nm and the 1881–1962 nm features, both corresponding with water features. A positive PC2 indicates the 2323–2490 nm and 2215–2256 nm region affinity, probably picking up small mineralogical variations due to the Al-OH, Fe-OH and Mg-OH bonds in silicate minerals. Whereas in the negative PC4 component, this 2150–2297 nm region (slightly larger) is

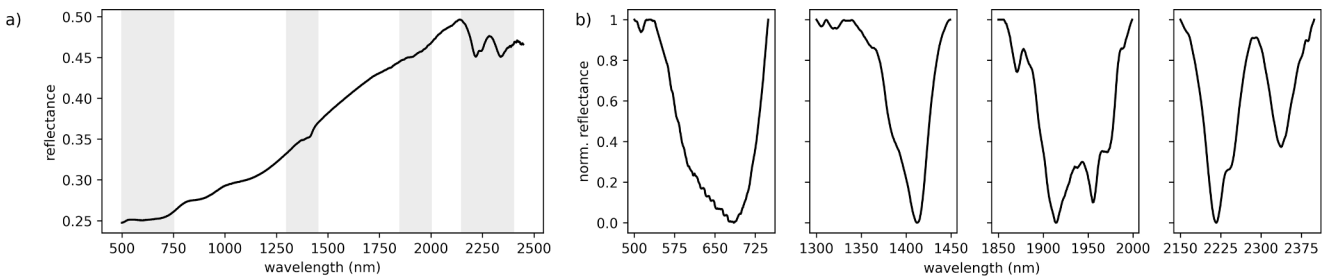

Fig. 6. Convex-hull removal of TerraSpec spectrum; (a) an example TerraSpec spectrum with the four selected regions used for clustering; (b) normalised hull-quotient spectrum for each region.

Table 1
Spectral sub-regions and characteristic absorption features used in this study.

Spectral feature	Defining characteristics of the feature extraction origin (Ausspec, 2008), description and classification if applicable (Roache pers. comm).	500–750 nm	1300–1450 nm	1850–2000 nm	2150–2400 nm
Fe-features	Fe-features, visible part of the spectra.	X			
w1400	Stretching vibrations of hydroxyl groups (OH). Within sheet silicates (kaolin group, white mica, smectite, chlorite), this is mostly located between 1390 and 1445 nm (Laukamp et al., 2021).		X		
w1900	Water features. The shape and intensity vary based on the mineral.			X	
wAlOH	Wavelength position of the Al-OH absorption feature (2205 ± 25 nm). Proxy for white mica composition. With longer wavelengths, substitution of Mg and Fe for Al into a more phengitic white mica.				X
wFeOH	Wavelength position of the FeOH absorption feature (2253 ± 15 nm). Proxy for chlorite composition. Mg-rich chlorite < 2252 nm, Fe-rich chlorite > 2252 nm.				X
wMgOH	Wavelength position of the Mg-OH absorption feature (2335 ± 25 nm). CO_3 and Mg-OH bearing minerals or secondary features of Al-OH.				X
Weathered/fresh	Ratio of the depth of Mg-OH and 1400 nm OH features. Used as a filter for weathered- and fresh material classification.		X		X
Sericite SWIR crystallinity	Ratio of the depth of Al-OH and 1900 nm H_2O feature. Increasing values represent increasing SWIR crystallinity of sericite, illite or kaolinite. The sericite crystallinity is useful to detect shear zones. The feldspars in high crystalline sericite are (almost) completely converted to white mica/sericite, whereas with lower crystalline values, significant remnants of the feldspars are still present (Ausspec, 2008; Dalm et al., 2014).			X	X
dAlOH/dMgOH	Ratio of depth Al-OH and Mg-OH features. It can be used for different purposes depending on conditions. 1) Rock type discrimination: higher values indicate relatively felsic rocks (>1.2), intermediate (0.8–1.2), lower values mafic (<0.8). 2) White mica vs chlorite/carbonate (or biotite): lower values indicate white mica + chlorite (biotite); at higher values, chlorite is negligible.				X
dMgOH/dFeOH	Ratio of depth Mg-OH and Fe-OH features. Measure of relative abundance of amphibole to chlorite (biotite). Amphibole > 3, biotite 2–3, chlorite < 2 (flexible).				X

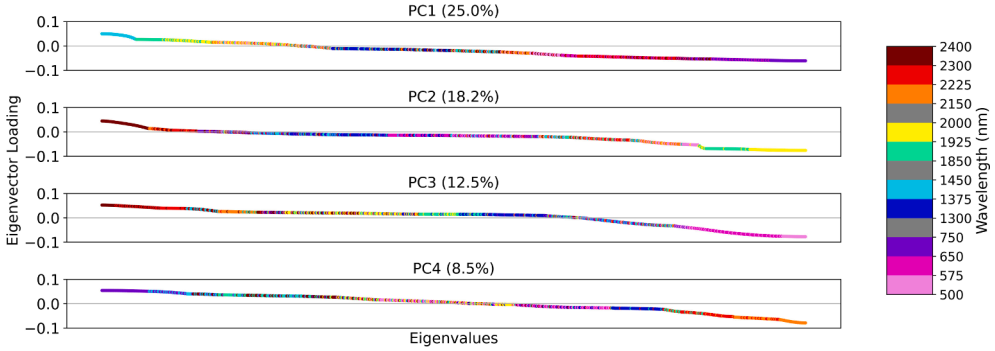

Fig. 7. Scaled and ordered eigenvalues of PC1–PC4 for the TS clustering input wavelengths (n = 800).

more related to the 1851–1872 nm and 1303–1354 nm region. This may show that vibrations picked up in these regions may be related to each other, and these relationships may not have been observed if only certain, closely constrained, wavelength and depth features were extracted. In addition, these (rather obvious) examples demonstrate that the proposed TerraSpec clustering approach produces viable results. Furthermore, almost every region has dominance in a PC at either the positive or negative eigenvalue extremes. This suggests that all wavelength regions influence separation of the TS samples. Supplementary Material Table A.1 contains an overview of the eigenvalues and loadings of all PCs.

The nineteen PCs were determined to represent the mineralogical signatures adequately and, thus, were subsequentially clustered using agglomerative hierarchical clustering (Wierzchoń and Kłopotek, 2018). It was found that the VNIR-SWIR features can best be partitioned in six, seven or eight clusters (or classes) indicated by the peak and trough in the mean silhouette score, Calinski-Harabasz index and Davies-Bouldin index (Aggarwal and Reddy, 2014) and clustering dendrogram (shown in Supplementary Material Fig. A.1 and A.2). It was chosen to select seven classes because a spatial contextual inspection showed that the additional separation (into TS classes 1 and 2) related to the weathered rock types that had been represented by only one class thus far. Eight classes would split TS class 3 which already had a fairly similar mineralogical composition to other classes. Further analysis of the classes is done using (1) histograms of the deepest absorption feature (Hecker et al., 2019) in each region, (2) results of analysing a subset of 31,489 samples using the TSG software and (3) spatial observations. Fig. 8 shows histograms of the wavelength at the maximum depth for several features per TS class and region and helps identify the main features separating and characterising the classes. Note that these classes resemble distinct mineralogical mixture patterns related to the gold-bearing material and accompanying dilution. Supplementary Material Fig. A.3 contains numerical overviews of other extracted VNIR-SWIR spectral features from the TSG sample subset.

Classes 1 and 2 comprise mostly of weathered material with clay-rich mineral phases and minor siderite (Table 2). Three main characteristics define these classes. Firstly, the histogram peak (Fig. 8) between 510 and 530 nm indicates that the ferric iron absorption bands (Fe-oxide intensity) typically observed in weathered material are more dominant than the other deepest absorption features around 600 or 700 nm (Zhou and Wang, 2017). Secondly, the weathered- and fresh-material indicator is low, indicating weathered material (Table 1). TS classes 1 and 2 have an average ratio between 1.3 and 1.4, whereas the other classes have a ratio between 2.5 and 5.0 (Supplementary Material Fig. A.3). Finally, these samples are found at shallow depths (<50 m) near the surface. Differences between the classes can be found in the mineral

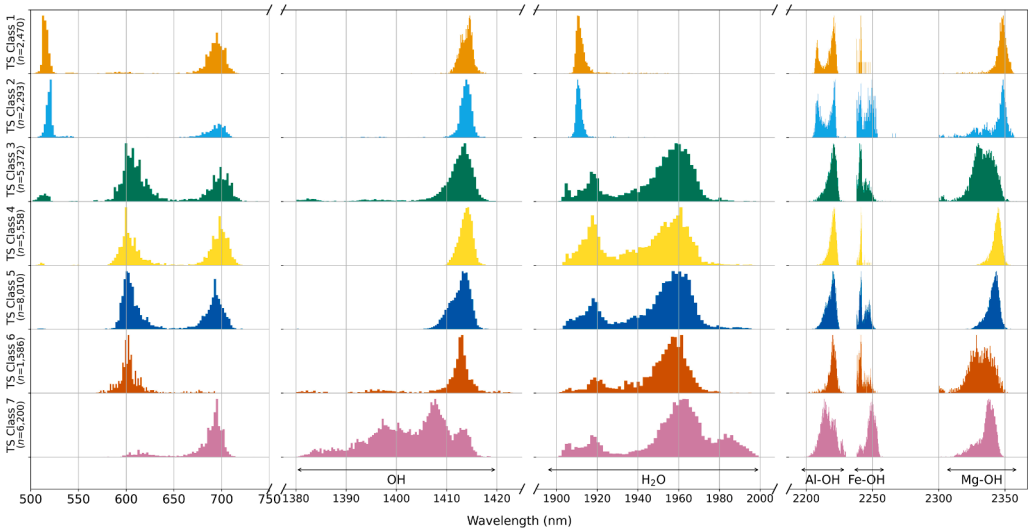

Fig. 8. Histograms of the wavelength at the maximum depth of the region 1, 1400 nm OH, 1955 nm H_2O, Al-OH, Fe-OH and Mg-OH absorption features for the TSG sample subset.

Table 2
Contingency table of the joint probability distribution (%) from the proportion of primary and secondary minerals in each TS class. Notation: <mineral1%>/<mineral2%>.

Mineral	TS class 1 n = 2,470	TS class 2 n = 2,293	TS class 3 n = 5,372	TS class 4 n = 5,558	TS class 5 n = 8,010	TS class 6 n = 1,586	TS class 7 n = 6,200
Phengite	36.4/8.4	12.5/5.4	47.5/28.4	96.8/2.8	87.8/9.4	48.8/22.4	24.7/32.4
Phengitic illite	42.8/9.2	28.6/8.5	0.3/0.1	0.8/-	0.4/-	-/-	0.1/0.1
Siderite	6.3/33.9	25.1/21.8	29.0/33.3	1.9/50.6	6.0/40.0	19.4/28.8	11.1/10.9
Montmorillonite	0.7/4.8	14.4/29.1	0.6/12.6	-/0.1	0.1/0.4	0.2/9.9	0.2/7.0
Chlorite-Mg	0.2/18.4	6.5/13.0	5.3/22.0	0.2/42.7	3.0/44.5	7.8/32.4	40.8/18.5
Chlorite-FeMg	0.1/-	0.9/0.4	0.6/0.5	-/0.4	0.9/1.9	0.2/0.7	17.5/6.1
Kaolinite-PX	9.5/20.5	7.4/15.5	-/-	-/0.1	-/-	-/0.1	-/0.2
Muscovite	0.6/0.5	0.5/0.1	0.7/2.1	0.3/0.1	1.6/1.2	0.9/4.3	1.2/13.9
Ankerite	-/0.7	-/0.7	-/0.1	-/2.9	-/1.9	-/0.2	-/1.6
Aspectral[1]	-/-	0.5/-	15.8/-	-/-	0.1/-	22.7/-	3.4/-
Other	3.4/3.6	3.6/5.5	0.2/0.9	-/0.3	0.1/0.7	-/1.2	1.0/9.3

[1] An aspectral response is a spectrum that does not match any of the library spectra. This could be due to a dark/noisy spectrum, mineral not in the library, a silicate mineral without any absorption in the SWIR (such as pyroxenes or feldspars).

composition, where TS class 1 has a phengite-illite-siderite composition and TS class 2 a phengitic-illite-montmorillonite composition. These classes may meaningfully influence processing behaviour as it will generally define softer but more clay-rich material.

Classes 3, 4 and 5 have white mica (phengite) as the dominant SWIR active mineral (Table 2), reflecting the mineralogy found in the K-feldspar and mica-dominated domains. Hence, the sericite crystallinity (definition in Table 1) can be used to differentiate their composition. The class compositions transition from a low SWIR crystalline white mica in TS class 3 (ratio = 2.15), followed by TS class 4 (ratio = 3.87) to

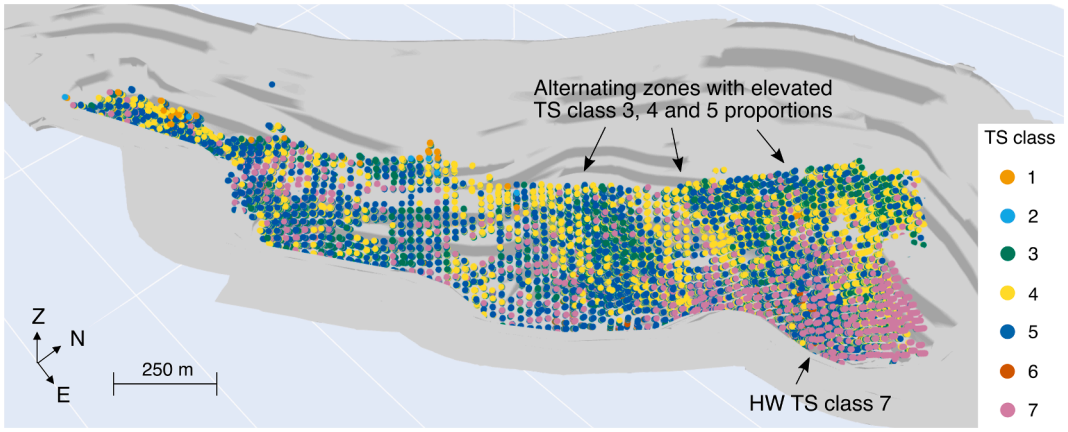

Fig. 9. Oblique view of the Tropicana pit displaying the pit outline in light grey with samples (n = 46,485) coloured by TS class. Alternating zones occur in SW to NE direction and by depth. HW: hanging wall.

a high SWIR crystalline white mica in TS class 5 (ratio = 4.81). This higher crystallinity would indicate that all feldspars are (almost) completely converted to white mica/sericite. This would imply less brittle material and being softer with regards to crushing. Yet resistive to milling given their capacity to absorb milling or grinding energy. With lower crystallinity, significant remnants of the feldspars are still present (Dalm et al., 2014). Spatially, these classes occur as larger domains alternating with each other (Fig. 9).

TS class 6 has a distinct shorter wavelength (600 nm) histogram and occurs as small lodes with a similar mineralogical composition to TS class 3 (phengitic-siderite-chloriteMg). These lodes are characterised by elevated sulphur concentrations (double compared to TS classes 4 and 5). Finally, TS class 7 discriminates waste rock (intrusion-related dilution within and surrounding the mineralised zone) as it is characterised by a low ratio of the dAlOH/dMgOH indices, where values < 0.8 indicate mafic rocks (Supplementary Material Fig. A.3). In addition, this class has a distinct Fe-OH absorption shoulder of chlorite around 2250 nm (Fig. 8), indicating the more mafic nature or rocks affected by chlorite alteration compared to the felsic rock-related mineralisation. Table 2 defines the primary mineralogy as chlorite-Mg (40.8 %) and chlorite-FeMg (17.5 %) with associated phengite (24.7 %).

4.1.1. Mineralogical features clustering summary

Most of the TS classes have at least one distinctive and characteristic feature which can be attributed to the mineralogy found within the mineralised zone. The composition and co-occurrence of the TS classes will be further explained where necessary in the subsequent sections. The benefit of this TS clustering using regions rather than a more common feature extraction will be demonstrated in Section 4.5. Additionally, feature extraction is not always possible because some spectra do not have any of the extracted features. This results in an incomplete data matrix, and missing value imputation must be done prior to clustering. The demonstrated approach is not affected since it only needs a normalised hull-quotient spectrum, which can always be generated from a spectrum. The TS classes were combined with the pXRF dataset into block features and clustered into material types as described in the next section.

4.2. Block feature PCA and clustering

After preparation of the block model and its features (Fig. 4), only blocks with more than three TS and pXRF samples were selected. This selection means that at least three 1 m composites describe the 12 × 12 × 3 m block composition. On average, there were between 3 and 4 TS samples and between 4 and 5 pXRF samples per block, and there were 19,201 blocks in total. Prior to clustering, the seven TS class block proportions and fifteen pXRF elemental concentrations (clr transformed) were transformed into fifteen PCs explaining 95 % of the data variance.

Fig. 10a shows the covariance biplot of the first two PCs, accounting for 34.5 % of the data variance. This shows the relation between the PCs and block features (represented as vectors) and links the features with the clustering classes (from now onwards, also called material types or MT). Each 12 × 12 × 3 m block is represented by a scatter point and is coloured by the material type (class). A few generalised features are evident from the biplot defined by similar vector orientation and magnitudes of the block features: (1) the positive PC1 loadings group of TS classes 1 and 2, Al and Si indicate weathered material; (2) a positive PC1 and PC2 contains the grouping of major elements, e.g., Fe, Cr, Mn, Zn, Ca, and TS class 7 which generally indicates more intermediate to mafic material. Within the mineralised zone, this would generally characterise (mafic) intrusion-related dilution; (3) the negative loading of PC2 with related K and Rb, and Zr and Nb indicate potassic alteration and a grouping of two relatively immobile elements, respectively. Together with (4) a negative PC1 and S, Pb, and TS class 3 loadings, this would indicate the most potassic rock types associated with higher-grade mineralisation.

The 19,201 block samples represented by fifteen PCs were clustered using agglomerative hierarchical clustering, resulting in nine material types (the classes). This number was determined to be optimal based on the mean silhouette score, Caliński-Harabasz index and Davies-Bouldin index, which are shown in Supplementary Material Fig. A.1. These metrics are commonly used in determining the optimal number of classes as they will measure the similarity of samples and resulting classes (Aggarwal and Reddy, 2014). In addition, a pre-screening of the resulting classes, including analysis of the clustering dendrogram (Supplementary Material Fig. A.4), was done to confirm they would make geological sense. Fig. 10b shows the block samples coloured by the resulting clustering classes and will be further analysed in the next section. The PCs, elemental concentrations, TS classes and extracted features, logged lithology, logged alteration, and spatial context (Section 4.3) were considered jointly to study the material properties of the identified material types.

4.2.1. Material types

A first impression of the material types (MT) is obtained by finding their relationship with the degree of mineralisation. Note that the Au concentration was not one of the clustering variables but that the Au

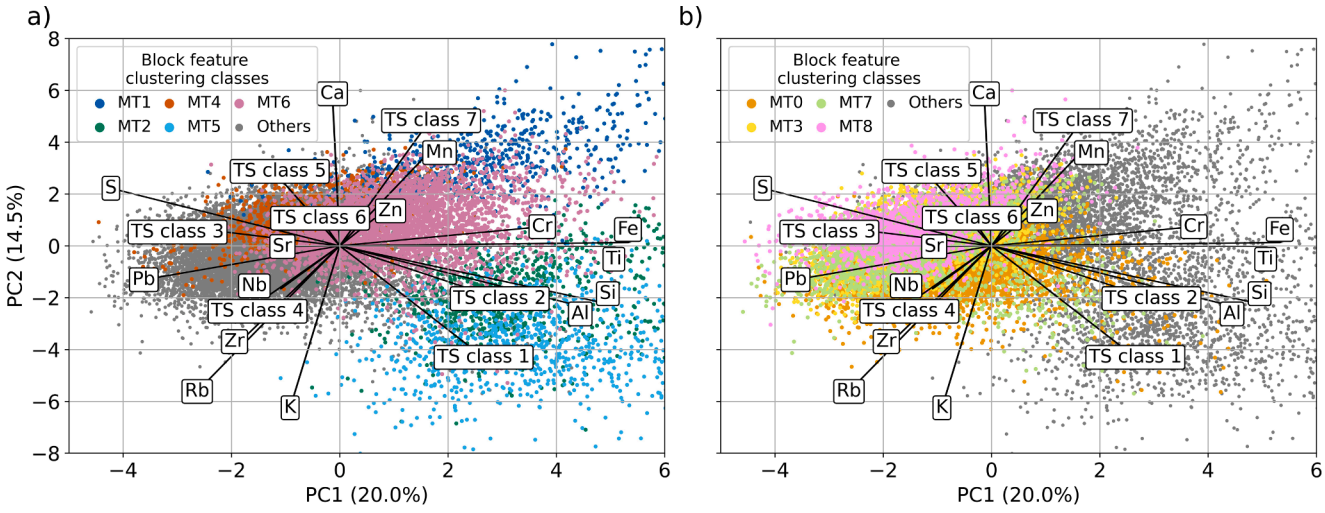

Fig. 10. Principal component covariance biplot of PC1–PC2 with the 22 block feature loadings. Blocks samples (n = 19,201) are coloured by the clustering classes (split for better visualisation).

content is used to define lower and higher-grade material types. The Au (ppm) boxplot in Fig. 11a shows that MT2 and MT5 have the lowest gold grade, followed by MT1 and MT6. Material types 0, 3, 7 and 8 resemble higher grade material.

Further insights into the mineralogical and geochemical composition of the material types are given using Fig. 11. The molar K/Al ratio (Fig. 11a) will be used to indicate the framework silicate modal mineralogy. Within the feldspathic gneiss units, lower values (<0.4) typically resemble a more plagioclase-rich feldspathic gneiss, whereas higher values (>0.4) indicate a higher perthite K-feldspar content (Hardwick, 2021). K-feldspar rich feldspathic gneiss samples (high K/Al) are more closely related to higher Au grade shoots (Blenkinsop and Doyle, 2014). The boxplots suggest that the material types can be divided into three categories: weathered types 2 and 5 (lowest Au grade), slightly higher Au grade, plagioclase-rich and non-feldspathic gneiss material types 1, 4 and 6 and high Au grade perthitic K-feldspar rich types 0, 3, 7 and 8. The following section will briefly discuss the main characteristics of each material type. More details are given while discussing the spatial contextual relationships (Section 4.2) and material hardness (Section 4.3).

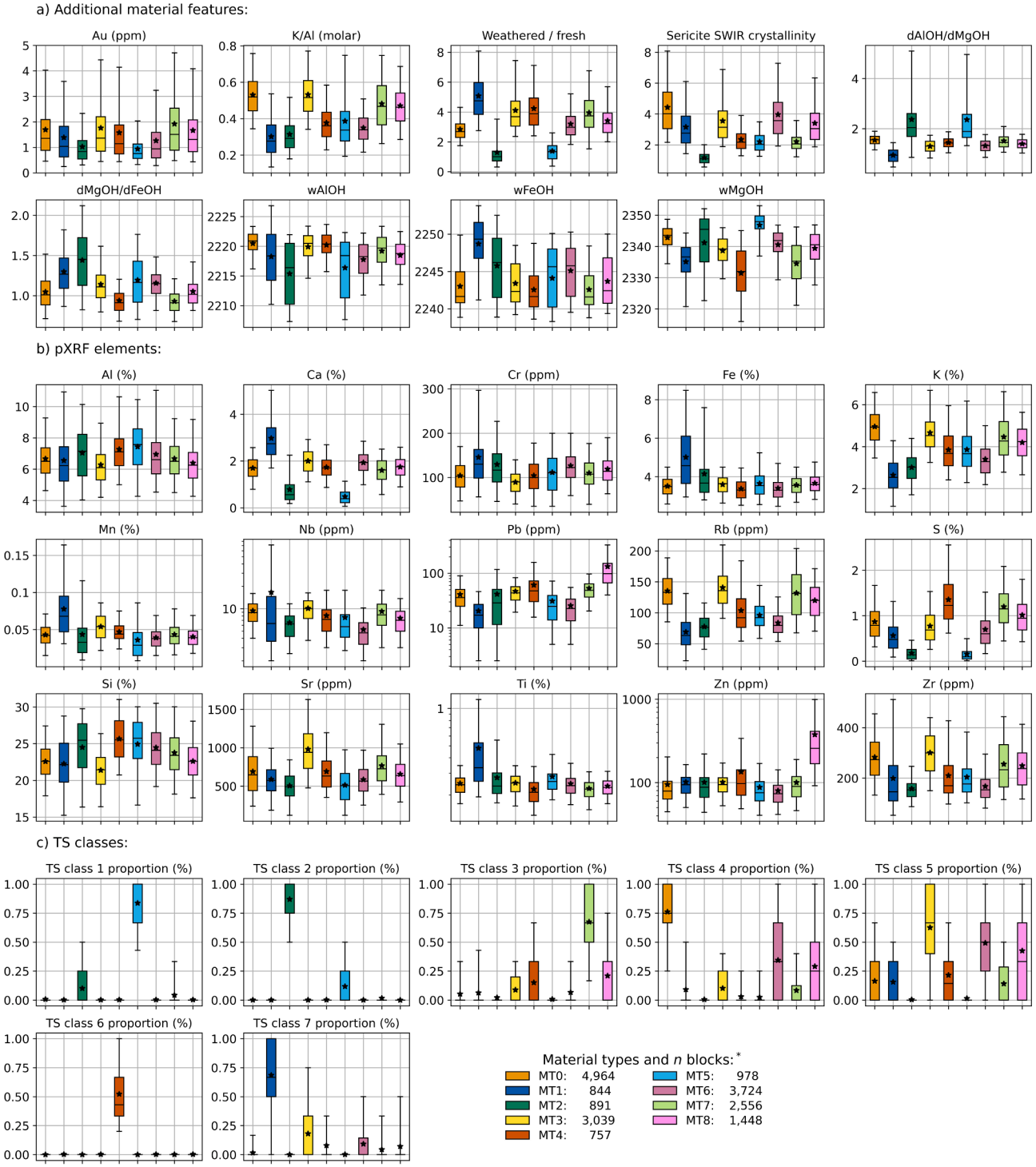

Fig. 11. Box and whisker plots of attributes of the block feature clustering blocks (n = 19,201); (a) Interpreted material features; (b) pXRF elemental concentrations; (c) TerraSpec (TS) classes. *The n blocks for part (a) are less as not all parameters are acquired for all blocks.

Material type 2 and 5 are two material types having significant weathering characteristics:

- Material type 2 (MT2, $n = 891$ blocks) and 5 are the only types with elevated TS classes 1 and 2 proportion, see Fig. 11c. This type is characterised by 87 % TS class 2 and 10 % TS class 1 and characterises a siderite-montmorillonite clay-rich upper saprolite unit. This material is slightly more weathered than material type 5, indicated by the weathered/fresh indicator (Table 1).
- Material type 5 (MT5, $n = 978$) has TS class proportions reversed to that of type 2: 12 % TS class 2 and 84 % TS class 5. This indicates a phengitic-illite-siderite with more kaolinite. Both material types have a low Ca and S concentration compared to the more elevated concentrations found in fresh rock, see Fig. 11b.

Material types 1, 4 and 6 were classified as being more related to plagioclase rich end-members of the feldspathic gneiss using the molar ratio of K/Al. A lower K/Al molar ratio may also imply lithologies different from feldspathic gneiss.

- Material type 1 (MT1, $n = 844$) is diagnostic with a high Ca, Fe, Mn and Ti, and has a distinct low K concentration, see Fig. 11b. This type is mainly characterised by TS classes 7 and 5 and display shifts to longer $>$ 2248 nm Fe-OH absorption wavelengths. These elemental concentrations and TS class signatures signify a more intermediate or mafic $\pm$ amphibolitic $\pm$ garnet gneiss with Mg-rich chlorite $\pm$ sericite-biotite alteration.
- Material type 4 (MT4, $n = 757$) is the only material type that is characterised using TS class 6, which characterises phengitic-siderite-chloriteMg mineralogy. This material has a high S and Si concentration but also has a distinct shorter 600 nm absorption peak (TS class 6). This diagnostic signature is not frequently found as it has the fewest blocks. The shift to longer wAlOH wavelengths and low K/Al (molar) suggest a more plagioclase rich feldspathic gneiss, but with a significant conversion of feldspars to phengite.
- Material type 6 (MT6, $n = 3{,}724$) is mainly composed of 49 % TS class 5 and 34 % TS class 4, indicating a phengite dominated material type. The lower K/Al ratio suggests that limited alteration took place, that this type slightly mafic is similar to material type 1, and lithological logging indicates that the feldspathic gneiss is amphibolite bearing and quartz-rich with a sericite-biotite $\pm$ chlorite alteration.

Material types 0, 3, 7 and 8 are closely related to higher-grade mineralisation (Fig. 11a) and indicates that Au grade-based domaining will not account for material variability. These types also have elevated K/Al molar ratios above 0.4 (Fig. 11a). These are more perthite-rich feldspathic gneiss material types having minor variations in mineralogical composition; however, the white mica is mostly phengitic in composition. Overall, these material types contain elevated concentration in K, Nb, Rb, S, Sr and Zr:

- Material type 0 (MT0, $n = 4{,}964$) is the largest material type and is characterised primarily by TS class 4 (76 %) and TS class 5 (16 %). It has longer 1400 nm OH features and a Mg-OH absorption shoulder around 2343 nm. It is assumed that this stronger Mg-OH feature is due to a higher proportion of biotite and minor chlorite.
- Material type 3 (MT3, $n = 3{,}039$) has a phengitic mineralogy identified by TS class 5 (63 %), but due to an elevated TS class 7 proportion, it also shows that some blocks relate with internal more mafic dilution within the mineralised zone. It has a more distinct H_2O feature around 1950 nm, whereas the other three types show variable wavelength positions. This type has the highest relative biotite content ($<$1.3 ratio of the Al-OH and Mg-OH absorption feature depths), relating to an Au-rich biotite-sericite altered rock type.
- Material type 7 (MT7, $n = 2{,}556$) is identified by a high proportion of TS class 3 (68 %), not seen in other material types. Some of the blocks have elevated smectite proportions indicating that this material type may be spatially closer to a lower saprolite unit. Overall, there is a relatively low SWIR crystalline white mica (Dalm et al., 2014), indicating that more remnants of the feldspar are still present.
- Material type 8 (MT8, $n = 1{,}448$) has a mineralogical composition characterised by a mixture of TS classes 3, 4 and 5, which means that it also has a mixed composition from material types 0, 3 and 7. This type is elevated in Pb and Zn, and has relatively shorter wAlOH (2218 nm) compared to the other three perthitic K-feldspar material types (2220 nm).

Previous work by the authors (van Duijvenbode et al., 2022) demonstrated how the proportionality of the material classes within the different orebody domains might explain the material hardness observed across the entire mine. The current work and material types aims to further explain the between and within material type differences. The smaller spatial context of each block particularly better represents the local material type conditions, which may allow for a more selective loading and hauling strategy.

4.3. Spatial context

To further understand potential hardness relationships within and between the different material types, it is important to consider spatial contextual relationships. Prior to this study, (van Duijvenbode et al., 2022) identified various orebody domains constrained by shear zones and the $\geq$ 0.3 ppm Au grade resource domains from the mine. In that paper, each domain was geochemically characterised using four acid digestion data, whereas this study uses pXRF and VNIR-SWIR data. The current study primarily focusses on the four domains defined within the Tropicana orebody region (their names are TP_1, TP_2, TP_3, and TP_4) also shown in Fig. 12. However, for reference, a spatial overview of all domains is given in Supplementary Material Fig. A.5.

Fig. 12a shows a three-dimensional representation of the Tropicana pit and the spatial configuration of the material types represented as blocks; Fig. 12b shows a 50 m thick section view and indicates the four different estimation domains defined based upon shears crosscutting the mineralised zone. These domains are similar to those used in van Duijvenbode et al. (2022) and refer to Supplementary Material Table A.2 for an overview of all average elemental concentrations and proportional TS class values per domain, including those not shown. The summary statistics of the domains show that blocks within the mineralised zone outline of TP_1 have proportions of 25 % MT0, 29.3 % MT3, 19.2 % MT7 and 12.9 % MT8. Transitioning to TP_2, the proportion of MT3 decreases by 10.6 % and MT6 and MT7 increase by 3.5 %, where the change in composition relates with a lower abundance of biotite (picked up by TS classes 3, 4 and 5) due to the shear zone. The material types indicate a more sericite-chlorite dominated zone rather than a biotite-pyrite dominated zone.

The mineralised zones at TP_3 and TP_4 are slightly deeper than TP_1 and TP_2 (Fig. 12b). The TP_3 domain has relatively similar characteristics to TP_1 and TP_2, but it has elevated Ca and K concentrations and decreased Fe, Ti indicating the transition to a more felsic (perthitic) K-feldspar and lower plagioclase proportions. TP_4 is located NE of the Jigger shear zone Fig. 1b. This domain has an elevated MT0 (44.2 %) proportion and a reduced MT8 (4.6 %) proportion. This difference is picked up by TS class 4 (49 %) and a lower TS class 5 proportion (28 %) together with an elevated S concentration. TS class 4 picks up longer Al-OH absorption wavelengths indicating a more perthitic K-feldspar rich and phengitic rock type.

The proportional co-occurrence of material type blocks across the other domains show similar differences between domains. For example, at Havana (Fig. 13a), MT0 and MT3 predominantly occur in the FW domain (named as HA_3), whereas at Boston Shaker, MT0 occurs in the

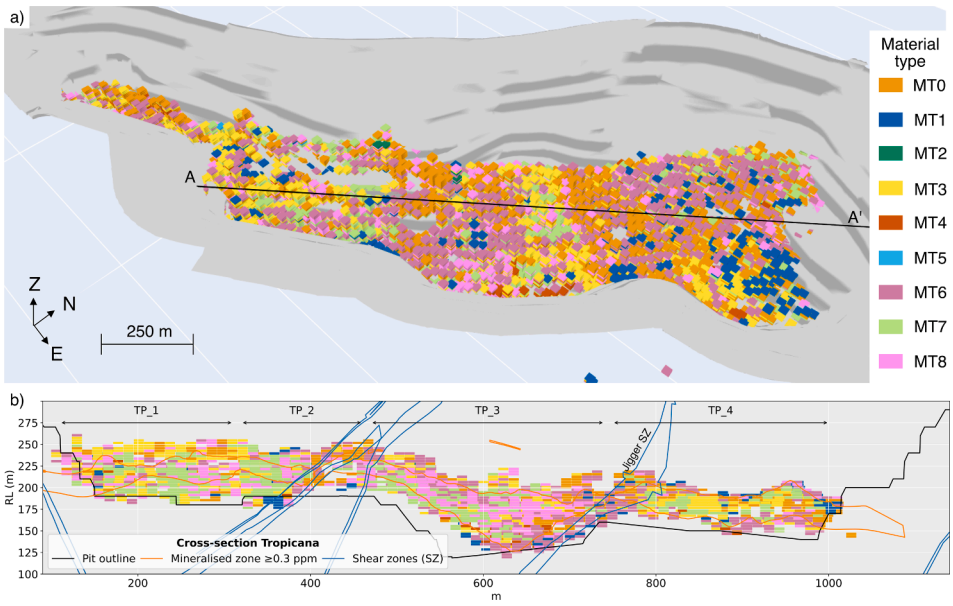

Fig. 12. Block model (12 × 12 × 3 m blocks) blocks coloured by material type class label; (a) oblique view of the Tropicana pit displaying the pit outline in light grey; (b) SW–NE 50 m thick cross-section along line A-A′.

HW domain (BS_2) and MT3 more in the FW (BS_1), although limited. Various material types are also found at different depths. For example, MT7 is found at Havana (Fig. 13a) near the bottom of the pit and characterises a phengitic K-feldspar rich domain (also with elevated sulphur, Fig. 5). Conversely, at Havana South (Fig. 13b) this domain is found closer to the surface, resembling a more smectite rich material type. MT2 and MT5 are also found closer to the surface, and MT1 and MT6 are more associated with the boundaries of the HW and FW. MT4 occurs as small lodes indicating a domain with elevated S, Pb and Zn.

4.4. Hardness proxy relationships

The spatial representation of material types is associated with different alteration assemblages, mineralogical compositions, elemental enrichments or depletions and textures. These properties define each material type, determine the physical properties and can therefore be used to identify hardness characteristics. The available legacy hardness proxies (penetration rate, Equotip, BWi and Axb) allow (Fig. 14) some preliminary hardness estimates to be made for each material type. For example, most of the weathered material (MT2 and MT5) has been mined out already, which means that the penetration rate (m/hr) provides a spatially wide-spread indication of the hardness. The weathered material is significantly easier (>100 m/hr) to penetrate (softer) than fresh rock (harder, <60 m/hr). Only subtle variations in the penetration rate occurs across the remaining material types. The softer rock character is also observed in the Equotip measurements, where MT2 has a Leeb hardness value of 642 ± 119 (mean ± 1 SD, only known in three blocks), while MT5 is not tested at all mainly due to friability of the drill core (weathered/oxidised core falls apart if tested). MT0, MT1, MT3 and MT6 have an Equotip hardness of 768 ± 64 Leeb, whereas MT4 and MT7 are slightly harder (799 ± 53 Leeb).

The BWi is a direct measure of the work index used to model the ball mill performance. This can be used to indicate the material hardness in terms of energy consumption required to grind the material from a given feed size to a specified product size (Lynch, 2015). Harder rocks require more energy to grind to the same target grind size than softer rocks. In

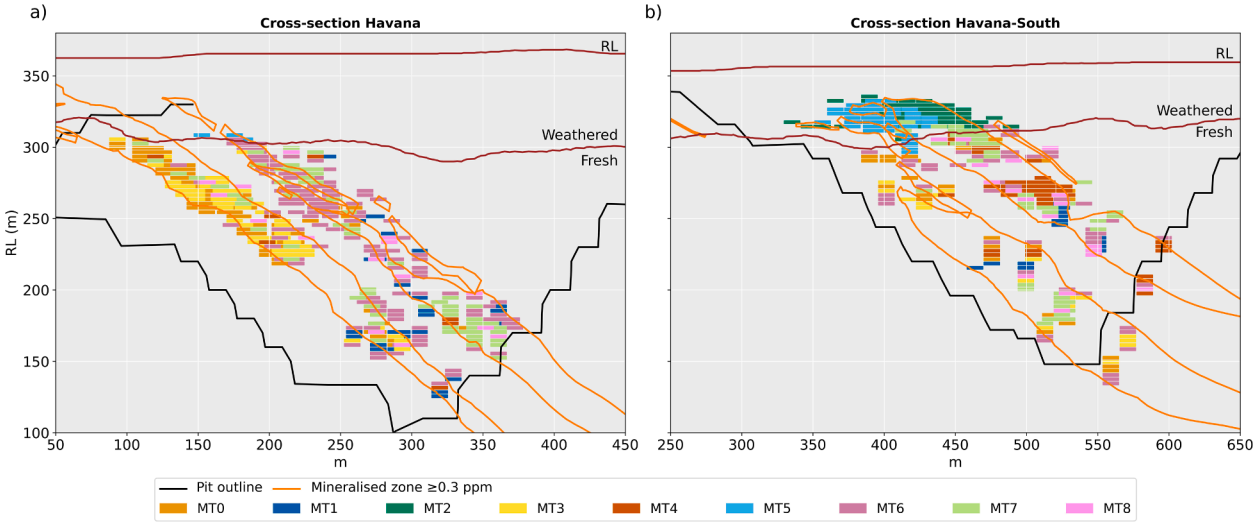

Fig. 13. Cross-section view 50 m thick; (a) Havana, section similar to Fig. 5; (b) Havana South section similar to displayed in Fig. 2, but moved 100 m parallel in SW direction.

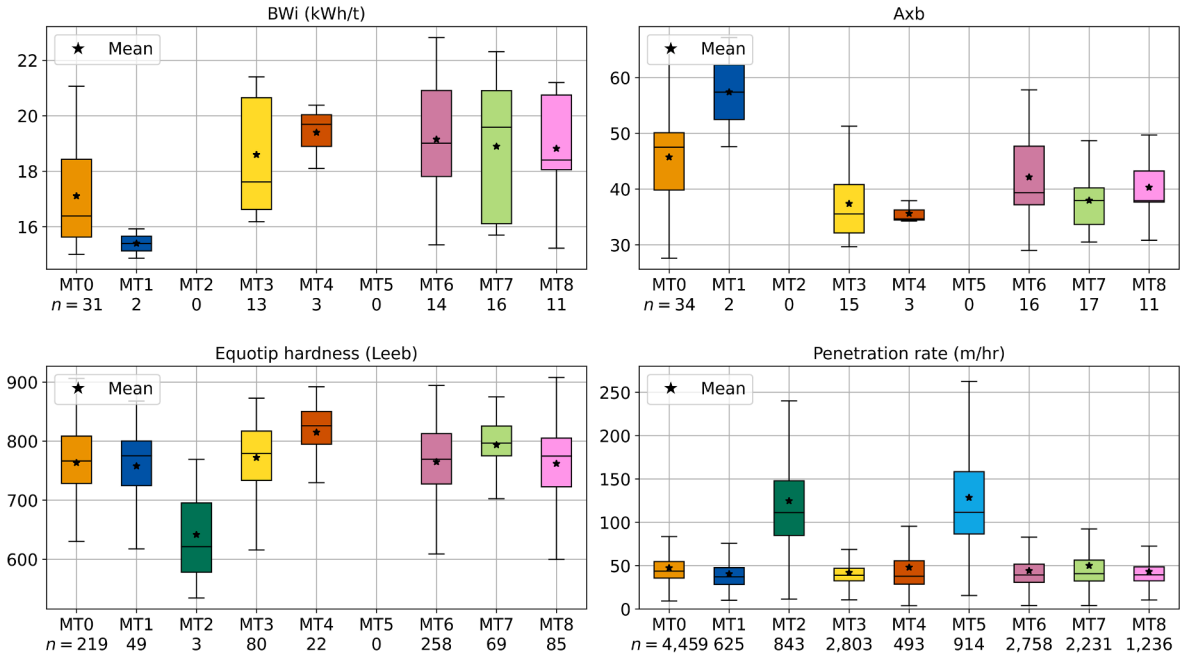

Fig. 14. Hardness characteristics per material type.

contrast, the Axb is a rock breakage parameter, where a higher value indicates that it is easier to break the rocks. Fig. 14 shows that especially MT3, MT4, MT6, MT7 and MT8 are harder than MT1 and MT0. At TGM, higher BWi, lower Axb are found in K-feldspar rich ore, whereas lower BWi and higher Axb are found in biotite-sericite ore, such as in MT0 (Roache, 2018). Section 5.1 will go into more detail about these hardness differences.

A lack of relevant hardness data resulted in there being insufficient co-located higher order hardness test data to effectively establish a robust, direct correlation of hardness with material types. However, the material types certainly constrain the expected hardness envelope as shown by the extend of the box and whiskers in Fig. 14 and insights of the characteristics of the material types. In theory, a preferred approach would obtain an additional material hardness estimate by determining a relationship between the Leeb hardness (Equotip) and BWi per material type. The more frequently (rapid and low cost) collected Equotip rebound hardness measurements, constrained to specific material types, can then be used to estimate the BWi and construct a hardness model. This hypothesis was tested earlier by (van Duijvenbode et al., 2021) but showed no correlation between the BWi and Equotip at TGM, possibly due to sub-optimal data collection/processing procedures, ineffective compositing and low sample representivity. However, extrapolating the material hardness has been demonstrated to be effective in other case studies. For example, a correlation between BWi and Equotip was determined in deposit types where a significant difference in material hardness is present, such as a BWi range from 5 to 18 kWh/t and associated Leeb values from 300 to 900 (van Duijvenbode et al., 2021). Typically such a correlation can only be found if due care has been taken to effectively constrain material composites used for higher-order hardness tests by distinct material types. The mineralised zones at TGM exhibit a relatively narrow hardness range between 15 and 20 kWh/t and 700–850 Leeb as this zone is only composed of a feldspathic gneiss rock composition which complicates the finding of Equotip – BWi correlations.

Furthermore, the summary statistics (Fig. 14) suggest within material type hardness variability. Ideally, classes could be further subdivided (e.g., for MT0, a Leeb value between 728 and 808 may relate with a BWi between 15.6 and 18.4 kWh/t) to potentially split into a softer and harder subclass (as shown in Section 5.1). This observation may seem strange because every material type already captures similar and distinct geochemical and mineralogical properties. However, clear explanations may be found in, for example, the texture, fabric and proportionalities of the material types. For example, various studies have shown the significant influence of the mineralised textures on the breakage behaviour of ores (e.g., Bonnici, 2012; Díaz et al., 2019). These affecting properties may lead to potential variations in hardness results depending on whether a destructive (BWi) vs non-destructive (Equotip) test is carried out. Exploring these within material type variabilities may be done using the VNIR-SWIR data and can further refine the hardness domains, as will be shown in the next section for an example at the Tropicana orebody region. Applying these domains to effectively constrain and target different material types may yield more conclusive comminution results.

4.5. *Within material type variability*

Specific VNIR-SWIR absorption features or regions can provide more information about the relative abundance and nature of mineral intergrowths related to mineral proportions, crystallinity and texture related hardness indications. For example, the relative proportion of white mica (wAlOH) could indicate sericitic vs feldspar dominated zones and thus provide macroscale-related mineralogical parameters (crystallinity, mineral composition) about the samples and the relation between Leeb hardness and BWi (hardness and brittleness).

The Tropicana orebody is a good location to investigate differences in mineralogical parameters, texture and their relationship with mineralogical composition. Fig. 15a shows an oblique three-dimensional representation of the Tropicana pit with some of the major shear zones crosscutting the deposit in E to SE direction (Blenkinsop and Doyle, 2014). The blocks are 12x12x3 m and are coloured by the BWi (kWh/t) corresponding to metallurgical composites found within the blocks. The northern end of the pit (TP_4) is bisected by the large Jigger shear zone (Fig. 1b) obliquely intersecting the line of mineralisation. There is softer material (~15–18 kWh/t) in the NE end compared to harder material (>20 kWh/t) in the SW. Another set of relatively softer blocks is found near the faults in the middle of Fig. 15a.

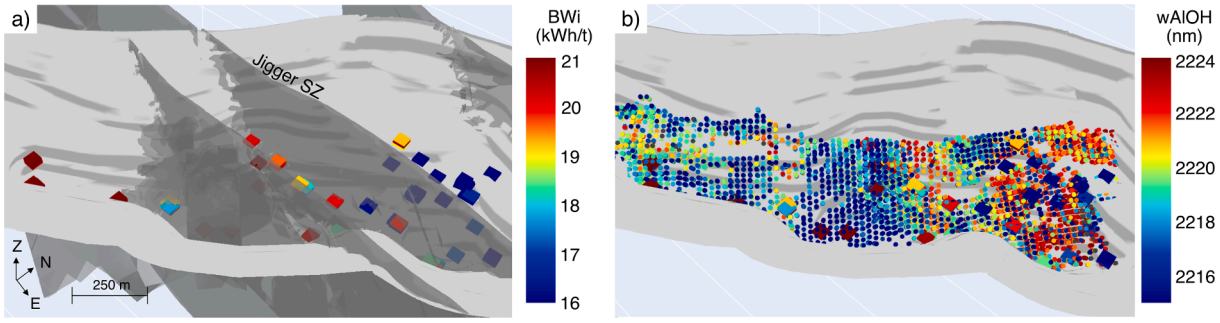

Fig. 15. Oblique view of the Tropicana pit displaying the pit outline in light grey; (a) major shear zones striking E to SE (dark grey) and blocks (12 × 12 × 3 m) coloured by BWi (kWh/t) corresponding with a metallurgical composite found within; (b) GC samples coloured by wAlOH.

It is possible to use the phengite distribution to model these shear structures and demonstrate a relationship between geology and the material domains.

Fig. 15b shows GC samples (within the ≥ 0.3 ppm Au zone) located within the blocks from Fig. 12. This shows that the shear feature and NE zone can be mapped by a larger relative proportion of phengite (wAlOH features > 2216 nm) in the SWIR data. The longer wavelength Al-OH suggests that there is not a discrete fault but rather a ductile zone (damage zone) comprised of multiple shears, as will be further discussed in the Discussion section. Texturally this rock has more schistosity and indicates a mica schist-dominated ore type (Roache, 2018). Thus, the phengite-rich rocks to the north of the shear zone, at TP_4 correspond to finer-grained, schistose material (less competent) whereas the relatively-low phengite concentrations in the SW imply harder K-feldspar-bearing material. In this context, the schist would be softer (milling) since there are more platy micas and structurally strained/sheared textures. The only problem is that the overall ore signature is also relatively phengitic (across all material types and deposits). Therefore, a mica-schist character would plot close to the mineralised zone spectra for white mica. Additionally, there are no major geochemical differences in a competent sample vs a sample having progressive foliation.

The white mica abundance shows a product of the alteration taking place in this domain and, in addition, at some locations, the white mica also indicates schistosity and thus a potential change in material hardness at TGM. The definitive relationship between white mica and texture is quite restricted in this context and is not yet extractable as a feature of the material types. Therefore, there is the necessity to understand geological structures to implement, for example, a white mica-schist texture proxy. For example, no elevated phengite proportion is found near the other faults displayed in Fig. 15. Reassessing the geochemical and mineralogical differences between the main material types in TP_3 and TP_4 (Supplementary Material Table A.2) showed a remarkable match between the normalised hull-quotient spectra in the 600–700 nm region and hardness domains primarily caused by the change in MT0 and MT8 proportion. There is a change in the wavelength of the deepest absorption feature in the 600–700 nm region in especially TS classes 3, 4, 5 and 6 (refer to Fig. 8 for the maximum depth locations). Therefore, this match may be useful to domain orebody hardness and predict the work index. There are also small variations in the average Nb, Zn, S and Mn concentration, however, these are not the explanation for the hardness variations.

Fig. 16 shows the average hull-quotient corrected spectra from the Tropicana domains. The average reflectance spectrum of TP_4 has its minimum absorption close to 605 nm, whereas the reflectance of the other domains has a more distinct minimum absorption around 690 nm. Commonly, this VNIR region is indicative of iron-bearing minerals (ferric iron (Fe^{3+}) absorption of hematite and goethite) or hydroxylated silicates with Fe, such as chlorite, biotite or epidote (Ausspec, 2008). Fig. 16 shows that this feature matches quite well with the hull normalised spectra of epidote in this region (Kokaly et al., 2017). The minimum absorption wavelength of epidote is around 618–620 nm, but within TP_4, this feature may have shifted slightly due to spectral mixing. This new w605 nm feature in combination with wAlOH indicates an epidote-phengite dominant ore type, which significantly correlates with softer material (low BWi) due to the shearing foliation.

The w605 feature of GC samples within the ≥ 0.3 ppm Au zone at Tropicana is visualised in Fig. 17 and coloured by the minimum absorption wavelength between 580 and 630 nm. This range is chosen because it captures the minimum absorption wavelength for the TP_4 ore around 605 nm ± 25 nm (w605 feature). A low w605 value indicates that there is a minimum within this zone and thus that the remaining hull-quotient spectrum increases, whereas a higher value (>625 nm) indicates that the minimum absorption will be at a higher wavelength (typically around 690 nm). Within the Tropicana orebody, a high w605 value and phengitic white mica composition correspond with significantly harder ore and vice versa.

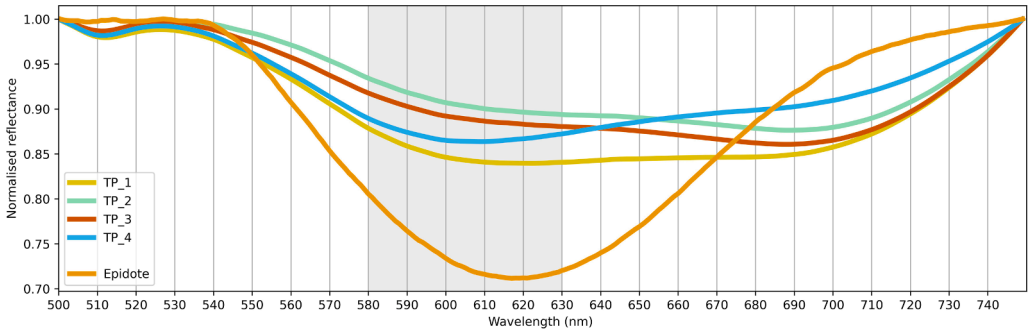

Fig. 16. Average hull normalised spectra from Tropicana domains. The spectrum of epidote (Kokaly et al., 2017) is provided as a reference for the identified 605 ± 25 nm feature within TP_4.

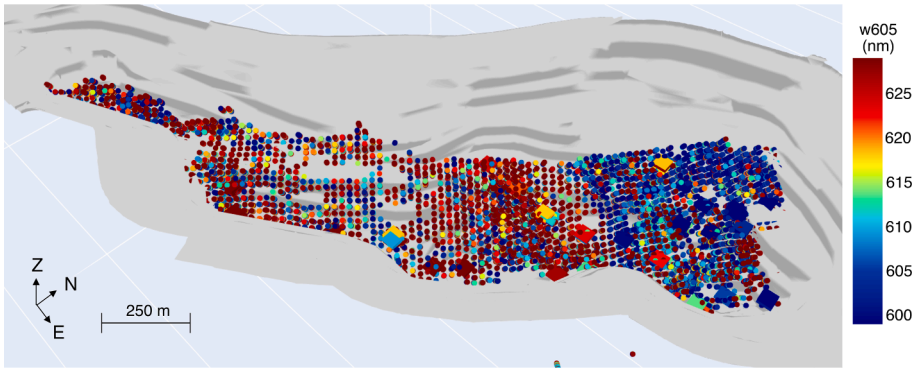

Fig. 17. Oblique view of the Tropicana pit displaying the pit outline in light grey and GC samples coloured by w605. Blocks are coloured by BWi (kWh/t), as in Fig. 15a.

5. Discussion

A relationship between the material types and hardness has been explored using a substantial data analysis. For instance, there were distinct mineralogical and geochemical differences in the predominantly weathered and fresh material types. However, as shown in Fig. 14, there was still variability in hardness within the specific material types. This variability may have been easier to separate in simpler deposit styles with more distinct rock types. At TGM, this was more complicated because the fresh mineralised rock is a felsic gneiss with various degrees of alteration and a significant mesoscale deformation history (Blenkinsop and Doyle, 2014). Therefore, the relationship between material type and hardness is more evident after including a spatial context which captures the rock deformations. This reveals the shared material type attributes (e.g., high wAlOH, low w605) within the larger domain. The revealed differences or commonalities within material types gave rise to the measured variations in hardness. These could then be used to subdivide the material types further. However, before that can be achieved, a deeper understanding of the material type composition is required, as was obtained by the block feature clustering approach.

It may be possible to better understand the hardness variability through geostatistical clustering (Fouedjio et al., 2017) or by including additional datasets such as penetration rate, Equotip or a proxy for texture. For instance, hyperspectral imaging of drill chips (from GC drilling) may add textural-structural, physical or other mechanical rock properties to the material types, as demonstrated by various other studies (e.g., Harraden et al., 2019; Koch et al., 2019; Schaefer et al., 2021). These additions may also give insight into geotechnical issues (mine design, slope stability) or drill and blast considerations (fly rock prediction, blast designs). The main limitation is that adding new variables may also reduce the number of block samples if enough measurements are not available. This may only be solved by improved correlations, more samples, or modelling of the geochemical, mineralogical and other proxies while considering the modelling limitations. In contrast, it would be preferable for daily operations to only use the geochemical and mineralogical data as this is already rapidly and routinely acquired (as done for TGM, see Section 3.1). These data may then be directly incorporated into a classification model that will determine the material type.

5.1. Material hardness and the w605 feature

A significant benefit of the material types with the w605 feature is that the types can be split into hard and soft components. For example, the 31 blocks of MT0 with BWi measurements of 17.1 ± 1.8 kWh/t (Fig. 14) can be split based upon an arbitrarily chosen w605 cut-off at 615 nm into a softer and harder part. The shorter w605 blocks ($n = 19$) have an average BWi of 16.6 ± 1.6 kWh/t, whereas the longer w605 blocks ($n = 12$) have a hardness of 17.9 ± 2 kWh/t. This separation is also true for the other material types, and the softer blocks normally have a higher wAlOH. Within the Tropicana pit, this feature splits the material into a softer (~15–18 kWh/t) and harder (>20 kWh/t) domain.

Epidote was indicated as one of the minerals associated with the softer sheared rock type found at TP_4. Typically, epidotes result from hydrothermal and metamorphic processes (Abweny et al., 2016) and form after various minerals, including feldspar, amphiboles, pyroxenes and micas, all present within the feldspathic gneiss at TGM. More evidence of this epidote feature was collected by analysing the diagnostic absorptions at 1550, 1830 and 2250 nm. There were relationships found between phengite + epidote at shorter 605 nm wavelengths and hornblende + epidote at longer 605 nm wavelengths. This would indicate that the newly found 605 nm feature is indeed one of the diagnostic features of epidote, but not exclusively limited to epidote. The wavelength position would change accordingly with the assemblage epidote sits in, which relates to the texture and resulting material hardness. This also explains why the deepest absorption features in Fig. 16 are not exactly at the same wavelength as that from epidote. Further research could focus on choosing an additional intermediate spectral range (1500–1850 nm) during the spectral clustering (Section 3.2) as this may help with mapping epidote and possibly discriminating it from other Fe hydrated silicates (biotite/chlorite).

The difference in BWi found at TP_3 and TP_4 has also been confirmed to be controlled by the mica content. The mineralised zone at TP_3 has a shorter wAlOH at 2217 nm, whereas TP_4 is at 2221 nm. Therefore, elevated epidote and phengite abundance correlate with short w605 and schistosity in paragenetic terms. On the other hand, relatively low abundance epidote + chlorite/biotite/amphibole are broadly associated with long w605 and static alteration of gneiss (Roache, pers. comm). This also applies to other domains. For example, the HW domain at Havana South (Fig. 13) has a phengitic white mica composition (wAlOH at 2219 nm) and short w605. However, this domain is more plagioclase-rich with epidote feldspar, thus having slightly harder material characteristics than the more perthitic K-feldspar at TP_4. The BWi (one composite only) is 18.4 kWh/t, and the average Equotip reads 795 Leeb.

5.2. Shear zone behaviour and structural geological control

Fig. 15a shows how the Jigger shear zone is modelled as a discrete fault plane intersecting the Tropicana orebody. However, the phengite-rich northern part of the pit suggests a wide, ductile sheared structure characterising an entire shear zone and not a discrete fault. In fact, the discrete planes do exist as a late brittle overprint but are filled with chlorite and smectite rather than phengite-biotite. The change in material composition and contribution to the change in hardness may be the result of feldspar-to-mica reactions occurring in these fault zones. During these processes, the released silica may have precipitated in the dilatant sites, increased the rock strength by cement hardening, and

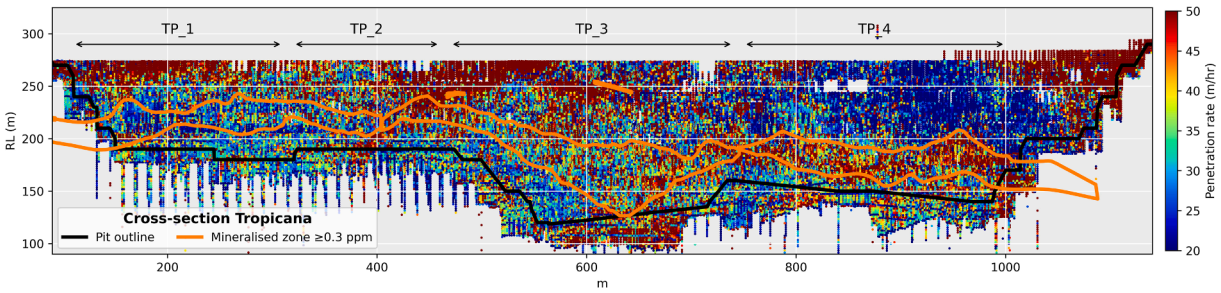

Fig. 18. Cross-section view through Tropicana (50 m thick, similar to Fig. 12) showing the penetration rate (m/hr) composited at 1 m intervals.

reduced permeability (the SW side). Whereas on the NE side, the transition of feldspars into phengitic (schist-like) micas may have been the dominant strength-controlling (softening) mechanism (Wibberley, 1999).

The resulting material hardness is a product of the feldspar-to-mica reactions described above, but also due to brittle-ductile transition periods after the peak high-grade metamorphic conditions (D3 and D4, Blenkinsop and Doyle (2014)). At the SW part of Tropicana, plagioclase broke down to micas which localises strain within anastomosing and only simple ductile shears. Whereas in the NE part, the K-feldspar has a more brittle response from the breakdown within an apparent low-strain and pure shear-dominated domain resulting in brittle deformation textures (Olierook et al., 2020). The current study demonstrates for the first time how the effects of shear zone processes are captured within the physical behaviour of material types. The kinematic effects on each type's material texture and hardness can be further split accordingly using the w605 (and wAlOH) features.

The formation and folding of the gneissic fabric at TGM was subordinate to the deformation history (Blenkinsop and Doyle, 2014) and resulted in the final material hardness of the rock before being mined. Blast hole drilling is the first activity affected by the material hardness and may therefore provide routine early proxies for hardness on a spatially dense scale. The between material type penetration rate average, excluding MT2 and MT5, was 44.8 ± 20.9 m/hr indicating that the mineralised zone has a fairly consistent hardness. Fig. 18 displays the penetration rate variability for the Tropicana cross-section shown earlier. The very hard region (<25 m/hr) above the TP_4 mineralised zone is a garnet-bearing quartzofeldspathic gneiss unit. The softer regions closer to the surface are affected by weathering. Note that penetration data for the first ~ 50 m was not available. The average penetration rate within the mineralised zone for TP_1, TP_2, TP_3 and TP_4 are 43.2, 45.1, 42.4 and 45.5 m/hr, respectively. The small but existing penetration rate difference suggests that the penetration rate can be used as an early hardness indication of the material to be processed. Especially, the spatial abundance and ease of obtaining this dataset benefit the fingerprinting of material types.

5.3. Implications of fingerprints

The fingerprinting methodology makes an important contribution to the synthesis and description of geological attributes by providing a new data layer that groups samples which underwent similar geological processes in an objective manner. The main rationale behind this approach is that each geological feature of the ore may have significance to some aspect of the operation. For instance, studying the individual hardness characteristics from classes (available for some of the samples) has proven to be indicative of the hardness of the entire class. The research showed that combining the material classes with spatial contextual relationships could largely explain any further physical transformations the material underwent, resulting in hardness changes. For example, the material located in a heavily sheared domain (Tropicana NE) tends to be softer due to more brittle behaviour exhibited during deformation. This brittle behaviour resulted in more fractures acting as fluid pathways giving locally more veining or gneissic banding. Other classes related to the oxides tend to be closer to the surface, being weathered and thus also showing softer characteristics. Finding the classes or class combinations that are more present in such regions, suggests an initial relationship which can be transferred and tested on regions with little knowledge about the deformation history.

Furthermore, material fingerprinting has a significant implication for preparing material blends for processing, as well as optimised metallurgical sampling and compositing for each material type. It has the ability to constrain alike material and specifically identify and target end-members in future test campaigns. The derived rough hardness envelopes would also be sufficient for informing longer term strategical decision-making. Finally, it is expected that one would readily detect these material types downstream and infer material characteristics (i.e., for ore/waste separation and material tracking).

6. Conclusion

Material fingerprinting at Tropicana Gold Mine has been used to demonstrate a link between rapidly acquired geochemical, mineralogical and hardness data (BWi, Axb, Equotip and penetration rate) of various material types. These linkages define fingerprints, which are proxies for the constitutive material hardness properties and provide a more comprehensive understanding of comminution behaviour. Each fingerprint was constructed by clustering pXRF data and spectral class proportion of samples found within a small block. Clustering of these block features resulted in nine classes representing different material types. These types showed between and within material type variability attributed to the elevation/depletion of geochemical concentrations, absence/presence of minerals, spectral features, hardness proxies and spatial contextual relationships.

The material fingerprinting revealed, amongst others, the following four attributes: (1) representative variations of plagioclase-rich or perthitic K-feldspar rich domains using the proportionalities of material types; (2) modifications of material types by overprinting alteration and deformations. This was discerned by the abundance/presence of chlorite, sericite or epidote within each material type; (3) spatial contextual relationships, which showed how the material types relate with the progressive breakdown of feldspar into phengitic white micas in zones of intense foliation; (4) how shear zone processes are captured within material types. Using the above, elevated epidote and phengite abundance were found to correlate with short w605 nm and schistosity. Conversely, relatively low abundance of epidote + chlorite/biotite are broadly associated with long w605 nm and static alteration of gneiss.

Considering the within material type variability, it was evident that the material hardness (BWi) matched with the newly recognised w605 nm region. The wavelength position changes accordingly with the assemblage epidote sits in, which relates to the texture and resulting material hardness. Additionally, this indicates the usefulness of the visible wavelength region. This feature could be utilised to separate material types into a softer (~15–18 kWh/t) and harder (>20 kWh/t)

material component. These results may be used for further domaining orebody hardness and processing response. The simple representation of material types with unique within material type variability gives a qualitative indication of the hardness abundance. The numerical data features (e.g., material type proportion, w605, wAlOH) would further enable interpolation of the data and allow easy visualisation and a quantitative hardness indication. Consideration of the interpretations and implications of the fingerprints enhanced the ability to use them to constrain end-member samples for metallurgical testing, material blend preparation and downstream optimisation opportunities.

CRediT authorship contribution statement

Jeroen R. van Duijvenbode: Conceptualization, Methodology, Software, Investigation, Writing – original draft, Visualization. **Louis M. Cloete:** Conceptualization, Methodology, Validation, Resources, Writing – review & editing. **Masoud S. Shishvan:** Conceptualization, Methodology, Validation, Supervision, Writing – review & editing. **Mike W.N. Buxton:** Conceptualization, Methodology, Validation, Supervision, Writing – review & editing.

Declaration of Competing Interest

The authors declare that they have no known competing financial interests or personal relationships that could have appeared to influence the work reported in this paper.

Data availability

The data that has been used is confidential.

Acknowledgements

The authors are grateful to AngloGold Ashanti Ltd. for permission to publish the outputs of the research and, in particular, to Vaughan Chamberlain for supporting this research. In addition, Tony Roache and Stephen Brown are thanked for their helpful input, which improved the paper. Finally, the anonymous reviewers are thanked for their constructive reviews, which considerably improved the paper.

Appendix A. Supplementary material

Supplementary data to this article can be found online at https://doi.org/10.1016/j.mineng.2022.107885.

References

Abweny, M.S., van Ruitenbeek, F.J.A., de Smeth, B., Woldai, T., van der Meer, F.D., Cudahy, T., Zegers, T., Blom, J.-K., Thuss, B., 2016. Short-Wavelength Infrared (SWIR) spectroscopy of low-grade metamorphic volcanic rocks of the Pilbara Craton. J. Afr. Earth Sc. 117, 124–134. https://doi.org/10.1016/j.jafrearsci.2016.01.024.

Aggarwal, C.C., Reddy, C.K., 2014. Data Clustering. Algorithms and Applications. Taylor & Francis Group, London.

Aitchison, J., 1986. The statistical analysis of compositional data. Monographs on Statistics and Applied Probability. Chapman & Hall, London.

Aitchison, J., 1999. Logratios and natural laws in compositional data analysis. Math. Geol. 31 (5), 563–580. https://doi.org/10.1023/a:1007568008032.

Arne, D., House, E., Pontual, S., Huntington, J., 2016. Hyperspectral interpretation of selected drill cores from orogenic gold deposits in central Victoria, Australia. Aust. J. Earth Sci. 1–23. https://doi.org/10.1080/08120099.2016.1223171.

AngloGold Ashanti, 2016. AngloGold Ashanti Lifts Tropicana Ore Reserve and Production Outlook, Perth, p. 42.

Ausspec, 2008. G-MEX Spectral Interpretation Field Manual. AusSpec International Ltd.

Bhuiyan, M., Esmaeili, K., Ordóñez-Calderón, J.C., 2022. Evaluation of rock characterization tests as geometallurgical predictors of bond work index at the Tasiast Mine, Mauritania. Miner. Eng. 175. https://doi.org/10.1016/j.mineng.2021.107293.

Blenkinsop, T.G., Doyle, M.G., 2014. Structural controls on gold mineralization on the margin of the Yilgarn craton, Albany-Fraser orogen: The Tropicana deposit, Western Australia. J. Struct. Geol. 67, 189–204. https://doi.org/10.1016/j.jsg.2014.01.013.

Bonnici, N.K., 2012. The mineralogical and textural characteristics of copper-gold deposits related to mineral processing attributes. University of Tasmania, Australia. Doctoral thesis,.

Booysen, R., Lorenz, S., Thiele, S.T., Fuchsloch, W.C., Marais, T., Nex, P.A.M., Gloaguen, R., 2022. Accurate hyperspectral imaging of mineralised outcrops: an example from lithium-bearing pegmatites at Uis, Namibia. Remote Sens. Environ. 269. https://doi.org/10.1016/j.rse.2021.112790.

Crawford, A.J., Doyle, M.G., 2016. Granulite-hosted gold: tectonic setting and lithogeochemistry of the tropicana deposit, Western Australia. Econ. Geol. 111 (2), 395–420. https://doi.org/10.2113/econgeo.111.2.395.

Dalm, M., Buxton, M.W.N., van Ruitenbeek, F.J.A., Voncken, J.H.L., 2014. Application of near-infrared spectroscopy to sensor based sorting of a porphyry copper ore. Miner. Eng. 58, 7–16. https://doi.org/10.1016/j.mineng.2013.12.016.

Deutsch, J.L., Palmer, K., Deutsch, C.V., Szymanski, J., Etsell, T.H., 2015. Spatial modeling of geometallurgical properties: techniques and a case study. Nat. Resour. Res. 25 (2), 161–181. https://doi.org/10.1007/s11053-015-9276-x.

Díaz, E., Pamparana, G., Voisin, L., Kracht, W., Martínez, P., 2019. Exploring the effect of the geological texture at meso and micro scale on grinding performance. Miner. Eng. 144. https://doi.org/10.1016/j.mineng.2019.106032.

Dominy, S., O'Connor, L., Parbhakar-Fox, A., Glass, H., Purevgerel, S., 2018. Geometallurgy — a route to more resilient mine operations. Minerals 8 (12). https://doi.org/10.3390/min8120560.

Doyle, M.G., Fletcher, I.R., Foster, J., Large, R.R., Mathur, R., McNaughton, N.J., Meffre, S., Muhling, J.R., Phillips, D., Rasmussen, B., 2015. Geochronological constraints on the Tropicana gold deposit and Albany-Fraser Orogen, Western Australia. Econ. Geol. 110 (2), 355–386. https://doi.org/10.2113/econgeo.110.2.355.

Fouedjio, F., Hill, E.J., Laukamp, C., 2017. Geostatistical clustering as an aid for ore body domaining: case study at the Rocklea Dome channel iron ore deposit, Western Australia. Appl. Earth Sci. 127 (1), 15–29. https://doi.org/10.1080/03717453.2017.1415114.

Hardwick, B., 2021. Mineralised textures at the Tropicana gold mine: Implications for the genetic model and deportment of gold. University of Tasmania, Tasmania. MSc.

Harraden, C.L., Cracknell, M.J., Lett, J., Berry, R.F., Carey, R., Harris, A.C., 2019. Automated core logging technology for geotechnical assessment: a study on core from the Cadia East Porphyry Deposit. Econ. Geol. 114 (8), 1495–1511. https://doi.org/10.5382/econgeo.4649.

Hecker, C., van Ruitenbeek, F.J.A., van der Werff, H.M.A., Bakker, W.H., Hewson, R.D., van der Meer, F.D., 2019. Spectral absorption feature analysis for finding ore: a tutorial on using the method in geological remote sensing. IEEE Geosci. Remote Sens. Mag. 7 (2), 51–71. https://doi.org/10.1109/mgrs.2019.2899193.

Hood, S.B., Cracknell, M.J., Gazley, M.F., Reading, A.M., 2019. Element mobility and spatial zonation associated with the Archean Hamlet orogenic Au deposit, Western Australia: implications for fluid pathways in shear zones. Chem. Geol. 514, 10–26. https://doi.org/10.1016/j.chemgeo.2019.03.022.

Johnson, C.L., Browning, D.A., Pendock, N.E., 2019. Hyperspectral imaging applications to geometallurgy: utilizing blast hole mineralogy to predict Au-Cu recovery and throughput at the Phoenix Mine, Nevada. Econ. Geol. 114 (8), 1481–1494. https://doi.org/10.5382/econgeo.4684.

Kazimoto, E.O., 2020. Short wavelength infrared spectral characterization of the mineralogy of Gokona and Nyabigena andesite-hosted gold deposits in North Mara, Tanzania. Tanzania J. Sci. 46 (2), 354–370.

King, G.S., Macdonald, J.L., 2016. The Business Case for Early-stage Implementation of Geometallurgy – an Example from the Productora Cu-Mo-Au Deposit, Chile. In: Third AusIMM International Geometallurgy Conference 2016. Australasian Institute of Mining and Metallurgy, Melbourne, Australia, Perth, Australia, pp. 125–133.

Koch, P.-H., Lund, C., Rosenkranz, J., 2019. Automated drill core mineralogical characterization method for texture classification and modal mineralogy estimation for geometallurgy. Miner. Eng. 136, 99–109. https://doi.org/10.1016/j.mineng.2019.03.008.

Kokaly, R.F., Clark, R.N., Swayze, G.A., Livo, K.E., Hoefen, T.M., Pearson, N.C., Wise, R. A., Benzel, W.M., Lowers, H.A., Driscoll, R.L., Klein, A.J., USGS Spectral Library Version 7. U.S. Geological Survey Data Series 1035, 2017, 61. https://doi.org/10.3133/ds1035.

Laukamp, C., Rodger, A., LeGras, M., Lampinen, H., Lau, I.C., Pejcic, B., Stromberg, J., Francis, N., Ramanaidou, E., 2021. Mineral physicochemistry underlying feature-based extraction of mineral abundance and composition from shortwave, mid and thermal infrared reflectance spectra. Minerals 11 (4). https://doi.org/10.3390/min11040347.

Lynch, A., 2015. Comminution Handbook. The Australian Institute of Mining and Metallurgy.

Michaux, S., O'Connor, L., 2020. How to set up and develop a geometallurgical program. GTK Open File Work Report, GTK, p. 237.

Molnár, F., OBrien, H., Lahaye, Y., Kurhila, M., Middleton, A., Johanson, B., 2017. Multi-stage hydrothermal processes and diverse metal associations in orogenic gold deposits of the Central Lapland Greenstone Belt, Finland. In: Mineral Resources to Discover–14th SGA Biennial Meeting, pp. 63–66.

Montoya, P., Keeney, L., Jahoda, R., Hunt, J., Berry, R., Drews, U., Chamberlain, V., Leichliter, S., 2011. Geometallurgical modelling techniques applicable to pre-feasibility projects — La Colosa case study. Proceedings of the International Geometallurgy Conference 103–111.

Ogunsola, N., Olaleye, B., Saliu, M., 2017. Effects of weathering on some physical and mechanical properties of Ewekoro Limestone, South-western Nigeria. Int. J. Eng. Appl. Sci. 4 (11), 257336.

Olierook, H.K.H., Rankenburg, K., Ulrich, S., Kirkland, C.L., Evans, N.J., Brown, S., McInnes, B.I.A., Prent, A., Gillespie, J., McDonald, B., Darragh, M., 2020. Resolving

multiple geological events using in situ Rb–Sr geochronology: implications for metallogenesis at Tropicana, Western Australia. Geochronology 2 (2), 283–303. https://doi.org/10.5194/gchron-2-283-2020.

Roache, T.J., 2018. Boston Shaker underground pre-feasibility: Geometallurgical domaining. In: Internal Report. AngloGold Ashanti Australia. Tropicana Operation 9.

Roache, T.J., 2019. aiSIRIS mineral interpretation assessment. In: Internal Report. AngloGold Ashanti Australia, Tropicana Operation, p. 13.

Rodger, A., Fabris, A., Laukamp, C., 2021. Feature extraction and clustering of hyperspectral drill core measurements to assess potential lithological and alteration boundaries. Minerals 11 (2). https://doi.org/10.3390/min11020136.

Schaefer, L.N., Kereszturi, G., Villeneuve, M., Kennedy, B., 2021. Determining physical and mechanical volcanic rock properties via reflectance spectroscopy. J. Volcanol. Geoth. Res. 420. https://doi.org/10.1016/j.jvolgeores.2021.107393.

Spaggiari, C.V., Kirkland, C.L., Pawley, M.J., Smithies, R.H., Wingate, M.T.D., Doyle, M. G., Blenkinsop, T.G., Clark, C., Oorschot, C.W., Fox, L.J., Savage, J., 2011. The Geology of the East Albany-Fraser Orogen - A Field Guide. Geological Survey of Western Australia.

van Duijvenbode, J.R., Buxton, M.W.N., Soleymani Shishvan, M., 2020. Performance improvements during mineral processing using material fingerprints derived from machine learning — a conceptual framework. Minerals 10 (4). https://doi.org/10.3390/min10040366.

van Duijvenbode, J.R., Cloete, L.M., Soleymani Shishvan, M., Buxton, M.W.N., 2021. Material fingerprinting as a potential tool to domain orebody hardness and enhancing the prediction of work index. In: Application of Computers and Operations Research in the Mineral Industry (APCOM 2021), The Southern African Institute of Mining and Metallurgy, Online, p. 12.

van Duijvenbode, J.R., Cloete, L.M., Soleymani Shishvan, M., Buxton, M.W.N., 2022. Interpreting run-of-mine comminution and recovery parameters using multi-element geochemical data clustering. Miner. Eng. 184. https://doi.org/10.1016/j.mineng.2022.107612.

Wambeke, T., Elder, D., Miller, A., Benndorf, J., Peattie, R., 2018. Real-time reconciliation of a geometallurgical model based on ball mill performance measurements – a pilot study at the Tropicana gold mine. Min. Technol. 127 (3), 115–130. https://doi.org/10.1080/25726668.2018.1436957.

Wibberley, C., 1999. Are feldspar-to-mica reactions necessarily reaction-softening processes in fault zones? J. Struct. Geol. 21 (8–9), 1219–1227. https://doi.org/10.1016/s0191-8141(99)00019-x.

Wierzchoń, S.T., Kłopotek, M.A., 2018. Modern Algorithms of Cluster Analysis. Springer.

Zhou, K.-F., Wang, S.-S., 2017. Spectral properties of weathered and fresh rock surfaces in the Xiemisitai metallogenic belt, NW Xinjiang, China. Open. Geosciences 9 (1). https://doi.org/10.1515/geo-2017-0027.